Received: 27 September 2022 | Revised: 12 October 2022 | Accepted: 22 October 2022
DOI: 10.22034/ecc.2023.363684.1533
Eurasian Chemical Communications
SAMI

FULL PAPER

Axial ligation for copper (II) complexes of bis (acetylacetonato) ethylenediimine and bis (3-chloroacetylacetonato) ethylenediimine

Israa A. Jassem[a] |Wathiq S. Abdul-Hassan[a,*] |Ibrahim A. Flafel[a] |Hussein O. Jghebil[b]

[a]*Department of Chemistry, College of Science, University of Thi-Qar, 64001 Nassiria, Iraq*

[b]*Thi-Qar General Directorate of Education, 64001 Nassiria, Iraq*

***Corresponding Author:**
Wathiq. S. Abdul-Hassan
Email: Wathiq.a_chem@sci.utq.edu.iq
Tel.: +9647745226201

In this work, the N_2O_2 ligands AN and AN-Cl and their copper (II) complexes CuAN and CuAN-Cl are prepared and characterized by mass, FTIR, UV-Visible absorption spectrometries, XRD diffraction, and thermal analyses. The reaction of copper complexes CuAN and CuAN-Cl with 4,4'-bipyridine at lab temperature afforded the five coordinated adducts CuANbpy and CuAN-Clbpy, respectively. Likewise, these adducts are formed in solution ($CHCl_3$ and DMF) and followed by absorption spectroscopy. The interaction of copper (II) complex with non-substituted bis-viologen $V_2^{2+}.2PF_6^{2-}$ are carried out in DMF media to afford the adducts CuAN-Cl. $V_2^{2+}.2PF_6^{2-}$. The novel molecular switch is obtained after reduction the viologen unites of this adduct in DMF media.

KEYWORDS

Bis (3-chloroacetylacetone) ethylenediimine; Bis (acetylacetone) ethylenediimine; 4,4'-bipyridine; Viologen; copper (II) complexes.

Introduction

A Schiff base, named after Hugo Schiff, is a molecule contains a functional group that has a carbon-nitrogen double bond, but the nitrogen atom is linked to an aryl or alkyl group rather than hydrogen [1]. The Schiff base bis(acetylacetone)ethylenediamine [4,4-(1,2 ethanediyldinitrilo)-bis(2-pentanone)] obtained from the condensation of two moles of acetylacetone and one mole of ethylenediamine has been shown to have an enaminoketone structure with intra-molecular hydrogen bonding both in the solid state [2] and in solution [3]. Due to the selectivity and high sensitivity of Schiff bases towards a variety of transition metal ions, where the Schiff base metal complexes were known more than 100 years ago, the interest in studying transitional element complexes prepared from Schiff bases has increased in recent years [4-7]. In the formation of metal complexes from the presence of an active donor group, azomethine, which can participate in the electron pair of a nitrogen atom in the formation of the coordination bond and the presence of other donating groups in compounds of transparent bases such as oxygen and sulfur, it is possible to behave as bidentate or triple ligands. There are numerous applications for tridentate, tetradentate, and polydentate homogeneous or heterogeneous donating atoms, bases, and their metal complexes. The ability of Schiff bases to coordinate divalent metal ions makes studies of these compounds even more important. The positions of the keto-enol, or amine-imine equilibrium, as well as the nature of the hydrogen bond in the six-membered chelate ring, are crucial in concerning these Schiff bases. Using bis-(acetylacetone)-ethylenediimine as the model compound, the forms I-III could be present in tautomeric equilibrium, as demonstrated, see equation 1.

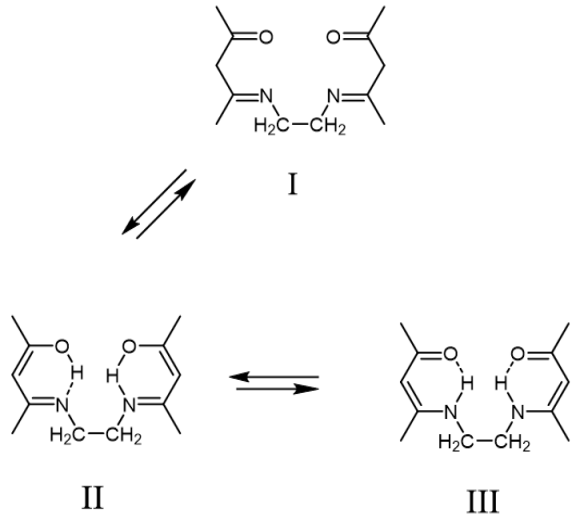

Equation 1 The tautomeric equilibrium forms of bis-(acetylacetone)-ethylenediimine

This study aimed to investigate the formation of the adduct complexes among each of bis (acetylacetonato) ethylenediimine Cu(II) and bis (3-chloro acetylacetonato) ethylenediimine Cu(II) with 4,4'-bipyridine (as solids and in solution) and dicationic propylene-spacered bis-viologen $V_2^{2+}.2PF_6^-$.

Experimental

Solvents and reagent

All the chemical materials and solvents used were of chemically pure, and commercially obtainable. Metal salt were used as acetate.

Physical measurements

The melting point of the ligand and metal complexes were determined in an electro thermal melting point device model (Melting SMP31). The FTIR spectra were recorded as Cesium iodide (CsI) for ligands and complexes using a Shimadzu FTIR spectrophotometer in the range (400-4000 cm^{-1}) (Model: IR- affinity, Shimadzu). Molecular weights were determined with Mass Spectra (MS) were registered in the range (0-800) were obtained by (Network Mass Selective Detector 5973).

Syntheses of bis (3-chloro acetylacetone) ethylenediimine (AN-Cl) and bis acetylacetone ethylenediimine (AN) [8]

Ethylenediamine (0.6 mL, 0.5315 g, 1eq) or (1.75 mL, 1.575 g, 1 eq) in 2 mL ethanol was added gradually with stirring to 3-chloroacetylacetone (2 mL, 2.38 g, 2 eq) or acetylacetone (5.4 mL, 5.292 g, 2 eq), respectively dissolved in 2 mL ethanol placed in ice bath. The resulting mixtures are stirred at lab temperature for 24 hours. The reaction mixtures are left to dry under air atmosphere, and then under vacuum. The produced precipitate AN-Cl was washed with distilled water. The obtained white solid AN was crystallized from water, and then washed with diethyl ether. The yields are 1.86 gm, 72 % (m.p. 134 °C) and 4.5 g, 76 % (m.p. 115 °C), respectively. IR(AN-Cl): 3136 υO-H, 3001 υC=C-H, 2958 υC-H, 1593 υC=N, 1554 υC=C, 1257 υC-O, 644 υC-Cl. IR(AN): 3151 υO-H, 3082 υC=C-H, 2958 υC-H, 1589 υC=N, 1516 υC=C, 1292 υC-O. For AN-Cl and AN. ESI-MS(m/z)= 293.1 $[M]^{\bullet+}$, 257.1 $[M-Cl]^+$.

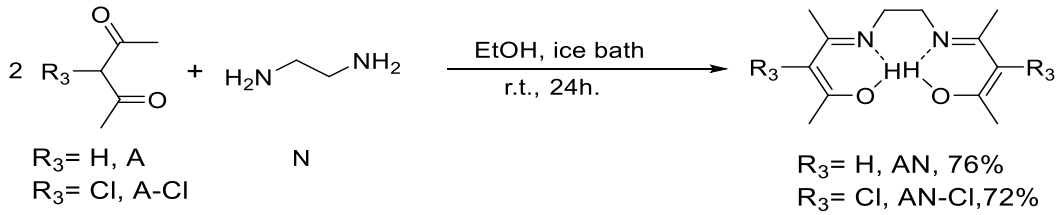

Syntheses of CuAN-Cl and CuAN

Over a period of 10 minutes, AN-Cl (0.6 g, 2.046 mmol, 1 eq) or AN (1 g, 4.458 mmol, 1 eq) dissolved in 4 mL methanol was added gradually with stirring to copper (II) acetate dissolved in 6 mL of distilled water-methanol mixture (1:1). The reaction mixtures are heated at 60 °C for 2 hours. Then, the reaction

mixtures are cooled in an ice bath. The resulted violet or blue precipitate of CuAN-Cl or CuAN, respectively was collected by filtration, washed with cold distilled water. After that, the precipitate was dried in an oven 100 °C to afford CuAN-Cl in yield of 0.7 g, 97 % or CuAN in yield of 1.05 g, 83 %. CuAN-Cl (m.p. 256 °C), FT-IR: 3001 υC=C-H, 2931 υC-H, 1558 υC=N, 1427 υC=C, 1273 υC-O, 624 υC-Cl, 459 υCu-N, 331 υCu-O. ESI-MS(m/z)= 354.7 $[M]^{\bullet+}$, 319 $[M\text{-}Cl]^{+}$. CuAN (m.p. 238 °C), FT- IR: 3012 υC=C-H, 2993 υC-H, 1577 υC=N, 1550 υC=C, 1273 υC-O, 455 υCu-N, 331 υCu-O. ESI-MS(m/z)= 285.8 $[M]^{\bullet+}$.

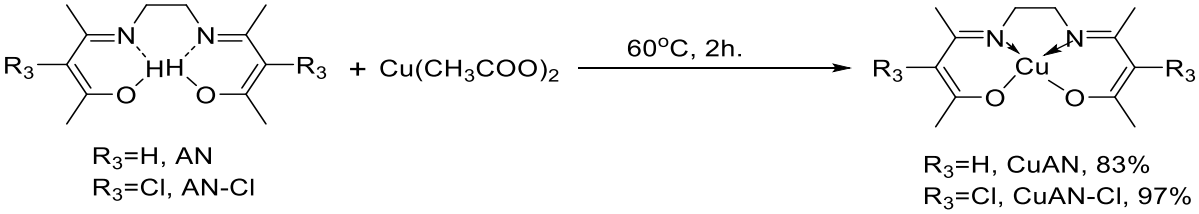

Syntheses of adducts=CuAN-Clbpy and CuANbpy

4,4'-bipyridine (2.19 g, 14.09 mmol) or (2.72 g, 17.49 mmol) was added to (0.5 g, 1.409 mmol) of CuAN-Cl or (0.5 g, 1.749 mmol) of CuAN dissolved in ~3 mL of ACN or $CHCl_3$ respectively. The Dark green-colored or light green-colored precipitates of the adduct were formed for CuAN-Cl. The light-green-colored precipitates of adduct complexes: CuAN-Clbpy or CuANbpy are immediately formed. The mixtures are stirred for ~24 hours. The precipitates are filtered and dried under vacuum. The yields are 0.51 g, 71% and 0.49 g, 64%, respectively. CuAN-Clbpy (m.p. 218 °C), FT-IR: 3001 υC=C-H, 2939 υC-H, 1566 υC=N, 1400 υC=C, 1273 υC-O, 617 υC-Cl, 455 υCu-N, 335 υCu-O. ESI-MS (m/z)= 510.9 $[M]^{\bullet+}$, 354.7 $[M\text{-}bpy]^{+}$. CuANbpy (m.p. 199 °C), FT-IR: 3039 υC=C-H, 2912 υC-H, 1585 υC=N, 1519 υC=C, 1265 υC-O, 424 υCu-N, 335 υCu-O. ESI-MS (m/z)= 442 $[M]^{\bullet+}$.

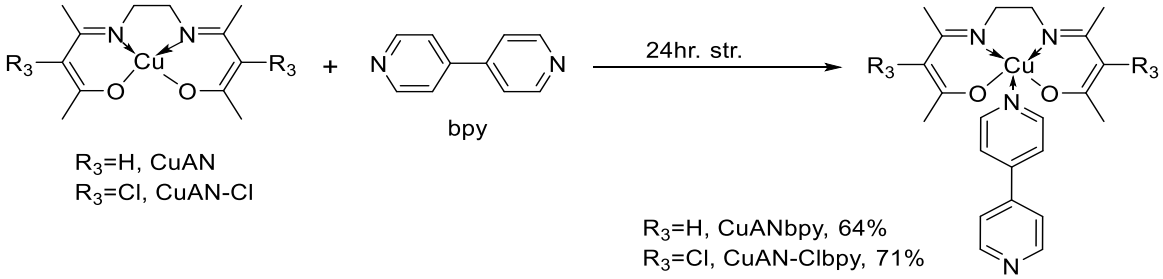

Results and discussion

Mass spectrometry

The mass spectra showed peaks at m/z = 293.1, 354.7, 510.9, 285.8, and 442 due to the molecular ions for AN-Cl, CuAN-Cl, CuAN-Clbpy, CuAN, and CuANbpy, respectively. The appearance of peaks at m/z = 257.1 and 319 indicate the loss of Cl radical for AN-Cl and CuAN-Cl, respectively. A peak at m/z = 354.7 indicate the loss of bpy for CuAN-Clbpy (Figures 1-5) [10].

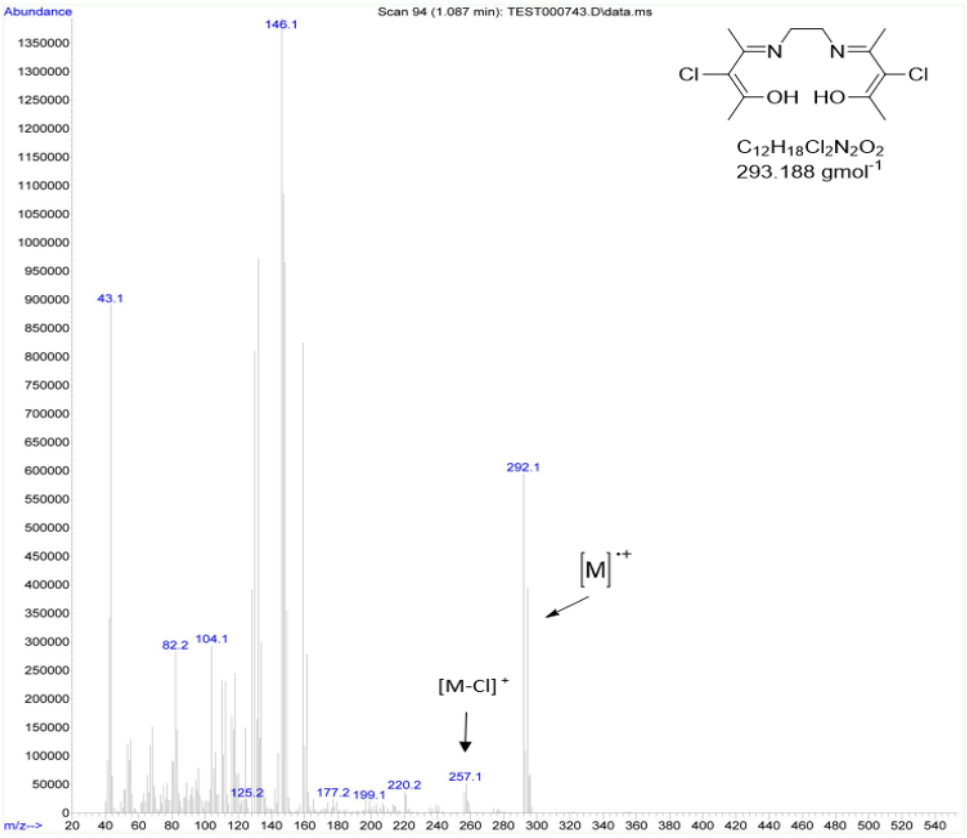

FIGURE 1 Mass spectrum of AN-Cl

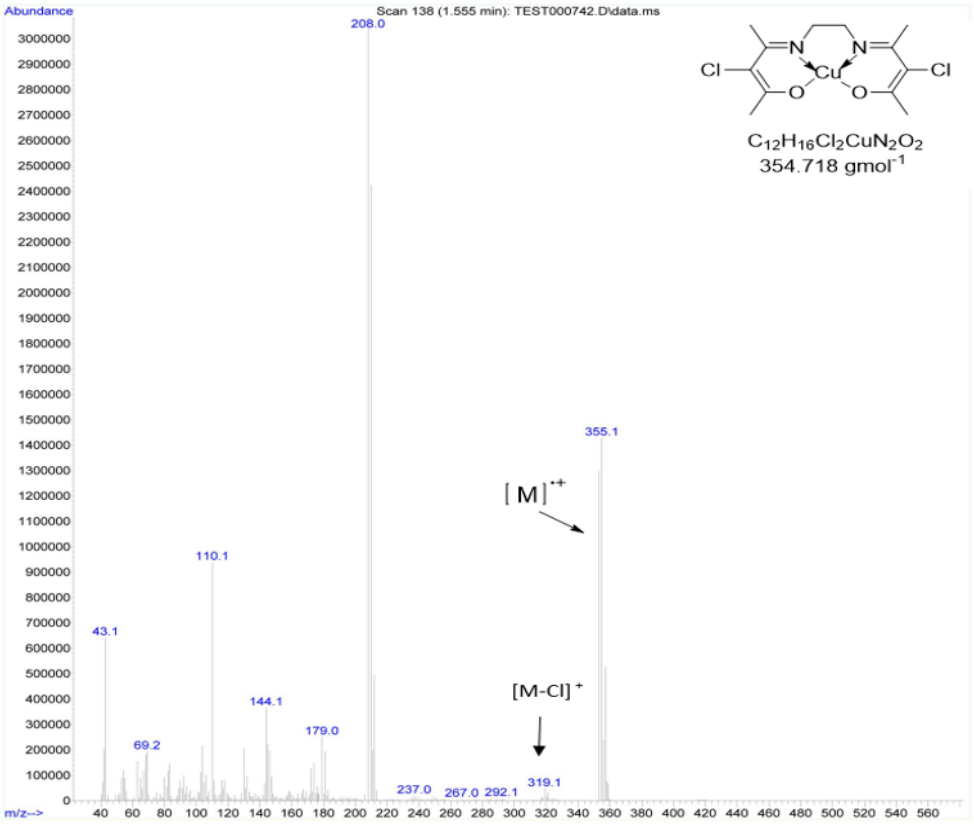

FIGURE 2 Mass spectrum of CuAN-Cl

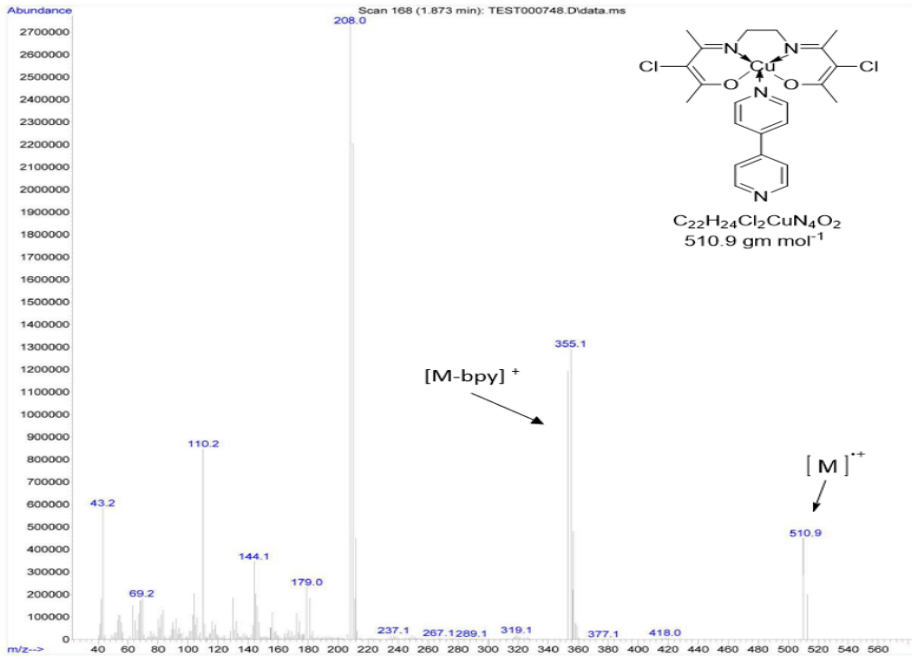

FIGURE 3 Mass spectrum of CuAN-Cl(bpy)

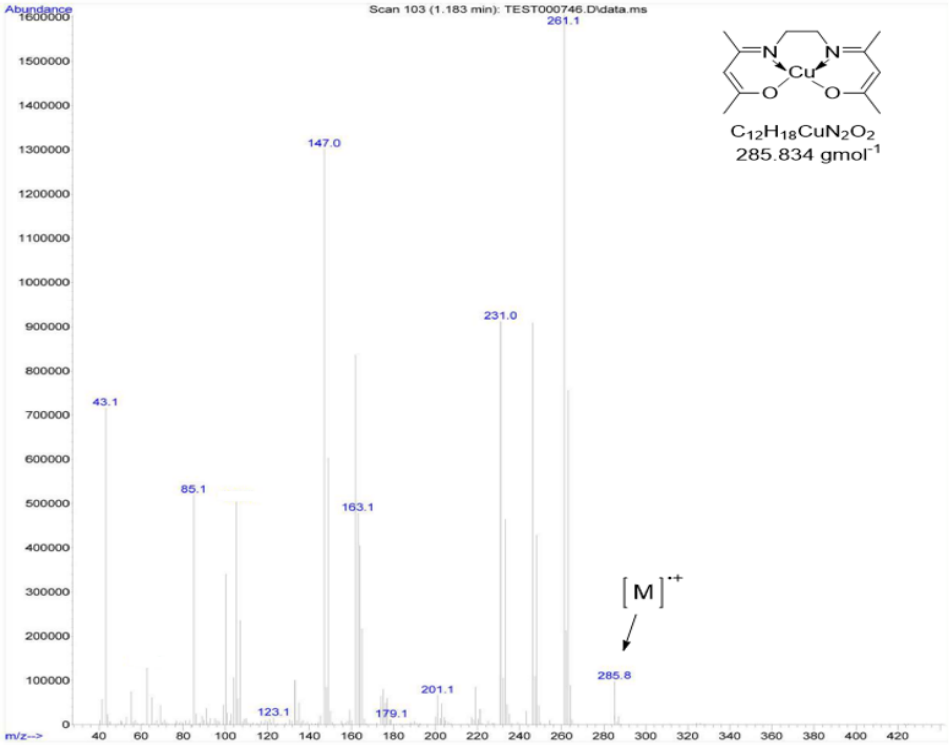

FIGURE 4 Mass spectrum of CuAN

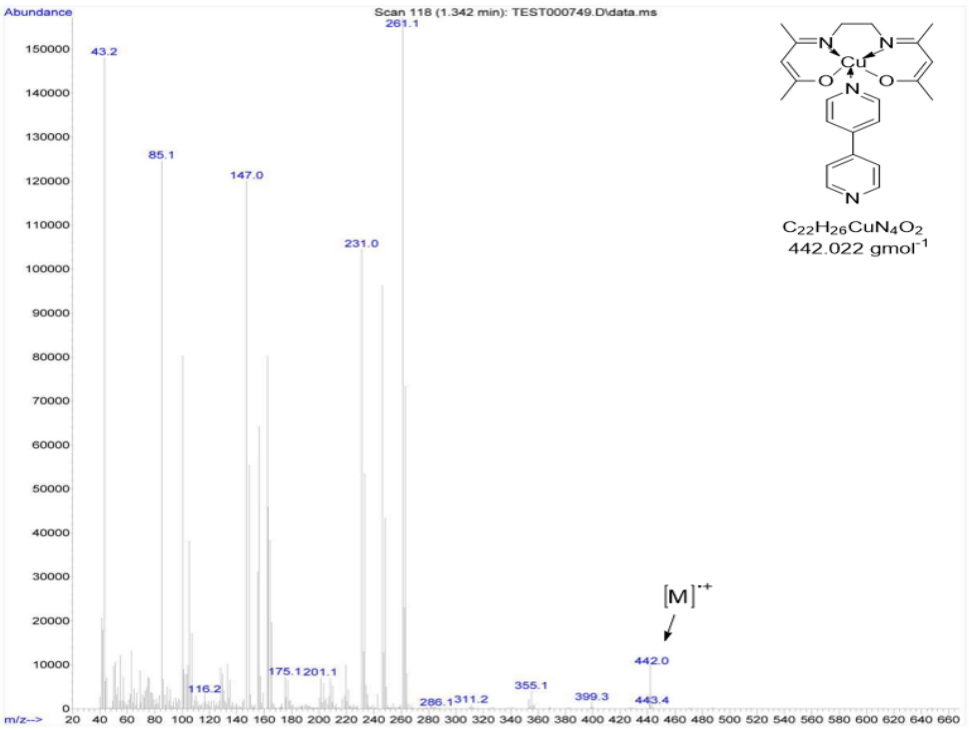

FIGURE 5 Mass spectrum of CuAN(bpy)

FT-IR spectrometry of ligands and their Cu(II) complexes

The FT-IR spectra are obtained for Shiff bases ligands and their complexes prepared as CsI discs. These spectra are presented in Figures 6-11. The most important FT-IR spectral data of AN-Cl, CuAN-Cl, CuAN-Clbpy, AN, CuAN, and CuANbpy have been summarized in Table 1. The FT-IR spectra of AN and AN-Cl showed bands at 3151 cm^{-1} and 3136 cm^{-1}, respectively which are attributed to the stretching vibrations of hydrogen bonded OH [11]. These bands disappeared in copper (II) complexes: CuAN and CuAN-Cl and their adducts: CuANbpy and CuAN-Clbpy which refer to de-protonation upon the complexation with Cu(II) matal ion. The OH bending vibrations of AN and AN-Cl appeared at 1292 cm^{-1} and 1257 cm^{-1}, respectively. The bands at 3082 cm^{-1}, 3012 cm^{-1}, 3039 cm^{-1}, 3001 cm^{-1}, 3001 cm^{-1}, and 3001 cm^{-1} occurred at AN, CuAN, CuANbpy, AN-Cl, CuAN-Cl, and CuAN-Clbpy, respectively are assigned to stretching vibrations of aromatic and/or olefinic C-H groups. While, the bending of these groups are noted at 736 cm^{-1}, 783 cm^{-1}, 756 cm^{-1}, 794 cm^{-1}, 702 cm^{-1}, and 752 cm^{-1}, respectively. The noted bands at 2958 cm^{-1}, 2920 cm^{-1}, 2912 cm^{-1}, 2958 cm^{-1}, 2931 cm^{-1}, and 2939 cm^{-1} are assigned to the stretching vibration of aliphatic C-H groups in AN, CuAN, CuANbpy, AN-Cl, CuAN-Cl, and CuAN-Clbpy. Whereas, the bending of these groups are noted at 1369 cm^{-1}, 1354 cm^{-1}, 1396 cm^{-1}, 1361 cm^{-1}, 1377 cm^{-1}, and 1346 cm^{-1}, respectively [12]. The stretching vibrations of C=N groups in AN and AN-Cl are noted at 1589 cm^{-1} and 1593 cm^{-1}, respectively [13]. These bands are blue shifted to be at 1577 cm^{-1}, 1585 cm^{-1}, 1558 cm^{-1}, and 1566 cm^{-1} in CuAN, CuANbpy, CuAN-Cl, and CuAN-Clbpy, respectively. The bands noted at 1585 cm^{-1} and 1566 cm^{-1} are assigned to the stretching vibrations of C=N in bipyridine moieties of CuANbpy and CuAN-Clbpy, respectively. The C=C [14] stretching vibrations happened at 1516 cm^{-1}, 1550 cm^{-1}, 1519 cm^{-1}, 1554 cm^{-1}, 1558 cm^{-1}, and 1566 cm^{-1} in AN,CuAN, CuANbpy, AN-Cl, CuAN-Cl, and CuAN-Clbpy, respectively. The stretching vibration of the C-O groups in AN and AN-Cl appeared at 1292 cm^{-1}, 1257 cm^{-1},

respectively. At complexation, these bands are shifted to be at 1273 cm^{-1}, 1265 cm^{-1}, 1273 cm^{-1}, and 1273 cm^{-1} in CuAN, CuANbpy, CuAN-Cl and CuAN-Clbpy, respectively [15]. The stretching vibration of C-Cl group in AN-Cl appeared at 644 cm^{-1}. These bands are blue shifted to be at 624 cm^{-1} and 617 cm^{-1} in CuAN-Cl and CuAN-Clbpy, respectively. The stretching vibrations of the coordination Cu-N bonds are seen at 455 cm^{-1}, 424 cm^{-1}, 459 cm^{-1}, and 455 cm^{-1} in CuAN, CuANbpy, CuAN-Cl, and CuAN-Clbpy, respectively. The bands noted at 331 cm^{-1}, 335 cm^{-1}, 331 cm^{-1}, and 335 cm^{-1} are assigned to the stretching vibrations of the coordination Cu-O bonds in CuAN, CuANbpy, CuAN-Clbpy, and CuAN-Clbpy, respectively. The noted differences in the stretching vibrations among the ligands AN and AN-Cl and their complexes: CuAN, CuANbpy, CuAN-Cl, and CuAN-Clbpy support well the complexation of Cu (II) metal ion with the groups C=N and C-O, i.e. the formation of the coordination bonds Cu-NC and Cu-OC, respectively.

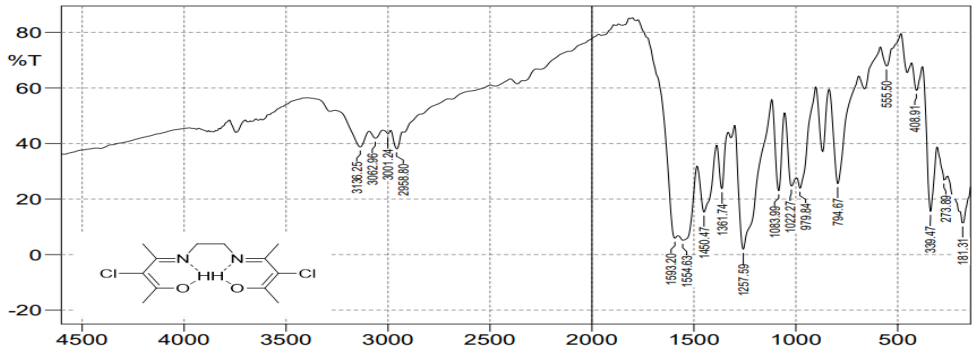

FIGURE 6 The FT-IR spectrum of ANCl ligand

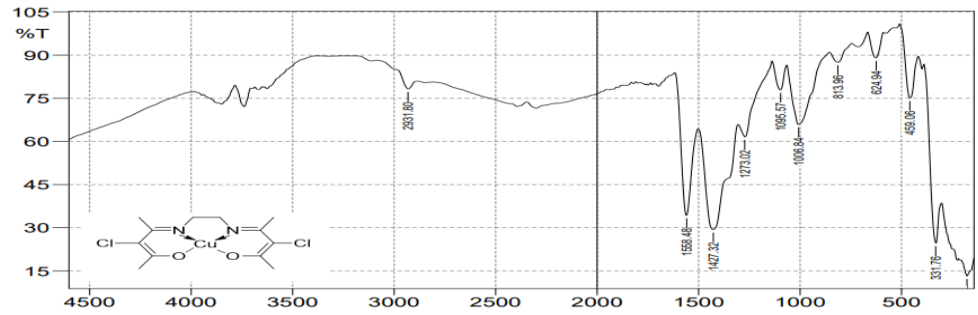

FIGURE 7 The FT-IR spectrum of CuAN-Cl complex

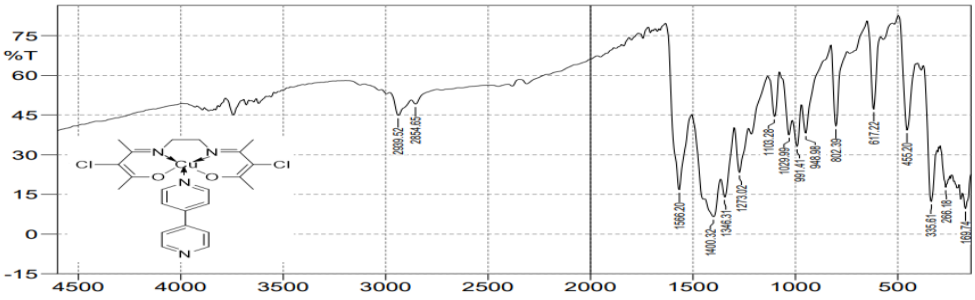

FIGURE 8 The FT-IR spectrum of CuAN-Cl(bpy) complex

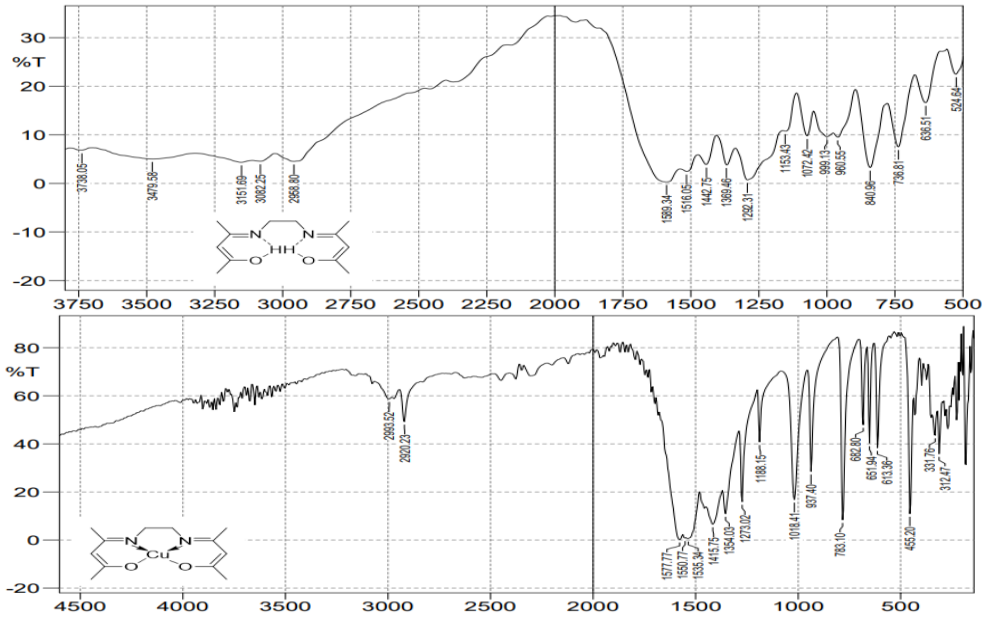

FIGURE 10 The FT-IR spectrum of CuAN complex

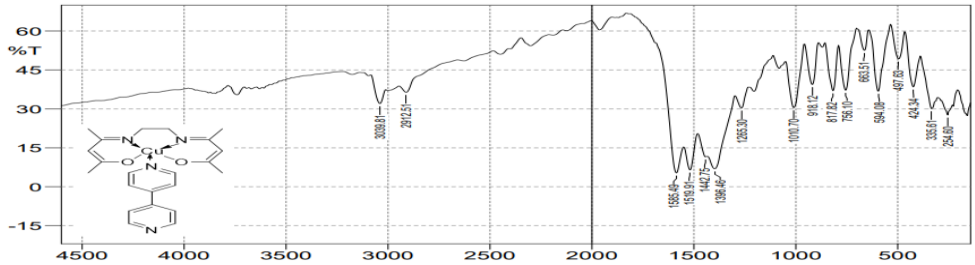

FIGURE 11 The FT-IR spectrum of CuAN(bpy) complex

TABLE 1 The FTIR data of ligands and their complexes

Wave number (cm^{-1})						Assignment
AN-Cl	CuAN-Cl	CuAN-Cl (bpy)	AN	CuAN	CuAN (bpy)	
3136	-	-	3151	-	-	υO-H
3001	3001	3001	3082	3012	3039	υC-H of aromatic and olefinic C=C-H
2958	2931	2939, 2854	2958	2993, 2920	2912	aliphatic ν C-H
1593	1558	1566	1589	1577	1585	υC=N
1554	1558	1566	1516	1550	1519	υC=C
1361	1377	1346	1369	1354	1396	aliphatic C-H bending
1257	1273	1273	1292	1273	1265	υC-O
1257	-	-	1292	-	-	C-OH bending
794	702	752	736	783	756	aromatic and olefinic C=C-H bending
644	624	617	-	-	-	υC-Cl
-	459	455	-	455	424	υCu-N
-	331	335	-	331	335	υCu-O

X-ray diffraction of the Cu(II) complexes

The X-ray diffraction was carried out for the complexes powders of CuANCl, CuANClbpy, CuAN, and CuANbpy. Their XRD patterns are within the range $10 < 2\theta < 80^{o}$ and are represented in Figures 12-15. The XRD

measurements proved that all the complexes were crystalline as they gave sharp peaks. Sherrer's equation (Equation 1) was used to calculate the average crystal size, as listed in Table 2.

Crystallite size, $Dp=K\lambda/(\beta \cos \theta)$…….. 1

Where, Dp is average crystallite size in nm. K is Scherrer constant (shape factor). Its value varies from 0.68 to 0.208. K= 0.94 for spherical crystallites with cubic symmetry. θ is the X-ray wavelength of radiation. For mini XRD, Cu Kα average = 1.5406 Å. β is full width at half maximum, FWHM of the peak in radians. θ is XRD peak position (diffraction angle), as one half of 2θ. [16] The Scherrer equation solely considers the effect of crystallite size on XRD peak broadening and does not account for lattice microstructures, such as intrinsic strain, which develops in nanocrystals via point defects, grain boundaries, triple junctions, and stacking faults. [17] The Williamson-Hall (W-H) method is one of the ways that considers the influence of strain-induced XRD peak broadening. This method calculates the crystal size as well as the intrinsic strain [18]. It is a combination of size and strain, according to the physical line broadening of the X-ray diffraction peak. This fundamental distinction aims for dissociation of broadening reflection and combines small crystallite size and micro-strain. In the W-H analysis, the distinct associations of both effects of size and strain broadening are given as Equation 3 and Table 2.

$\beta \cos \theta = K\lambda/ Dp + 4 \text{Ɛ} \sin \theta$ 3

The 4 sin θ is plotted (x-axis) versus the β cos θ (y-axis), see Figures 16-19. The fitted line's slope and intercept appear to be related to the strain and crystal size, respectively. The intercept value is equal to $K\lambda/ Dp$ and the slope value is equal to Ɛ. The units of 4 sin θ and β cos θ are degree and radian degree, respectively, in this plot [19-21].

First of all, the differences in peak numbers, intensities, Dp values and Ɛ values support the formation of the adducts from their precursor complexes. The largest peaks are noted for CuAN-Cl at 11.009510, 24.076170, 36.712360, 26.729480, and 43.337910 for CuAN-Cl(bpy) at 10.2988 22.6819, 17.5143 11.9552, 13.3150, and 24.6042 and for CuAN at 11.7170, 12.1188, 17.4460, 15.8979, 27.5718, and 24.9730 for CuAN(bpy) at 11.4942, 17.2539, 12.5202, 24.6319, 30.165, and 16.4079. Both these two methods showed that CuAN-Cl, CuAN-Cl(bpy), CuAN, and CuAN(bpy) complexes are in nano-crystal sizes: 18.76 nm, 29.80 nm, 28.40 nm, and 35 nm from Scherrer equation and 33.37 nm, 60.85 nm, 23.98 nm, and 33.68 nm from Williamson-Hall, respectively. The Ɛ values are calculated from the slope of the Williamson-Hall relationships and were 0.00417, 0.00393, -6.2568×10^{-4}, and -1.03869×10^{-4} for CuAN-Cl, CuAN-Cl(bpy), CuAN, and CuAN(bpy), respectively. Positive intrinsic strain values indicate tensile strain, while negative intrinsic strain values indicate compressive strain. The XRD patterns of the five coordinated adducts CuAN-Cl(bpy) and CuAN(bpy) were with obvious more peaks and highest intensities compared with XRD patterns of their precursors four coordinated complexes (at square geometries): CuAN-Cl and CuAN, respectively. Likewise, it was noted that the FWHM values were high for most of the peaks.

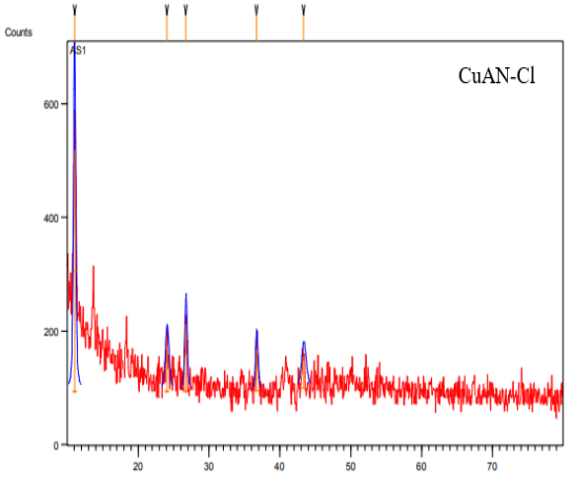

FIGURE 12 The XRD pattern of CuAN-Cl

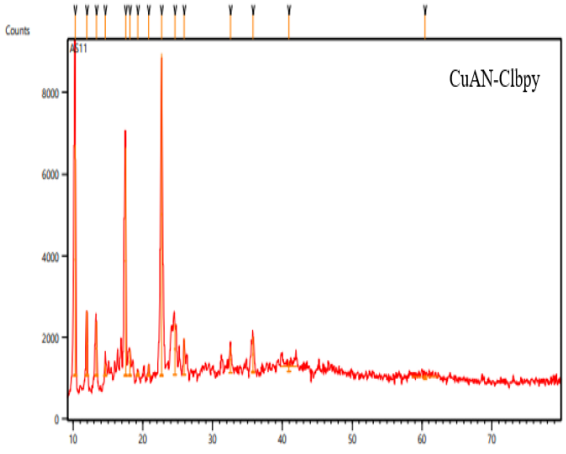

FIGURE 13 The XRD pattern of CuAN-Cl(bpy)

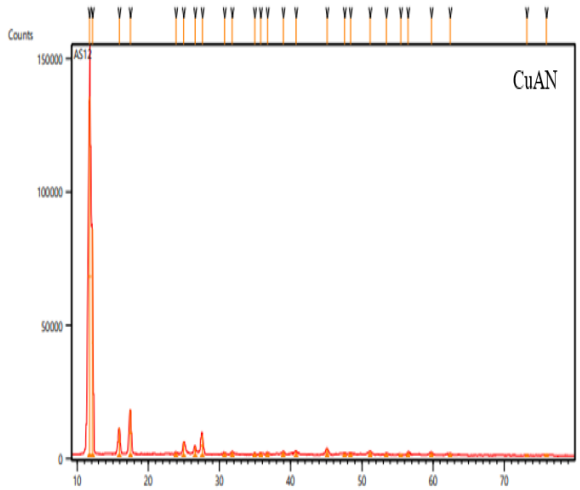

FIGURE 14 The XRD pattern of CuAN

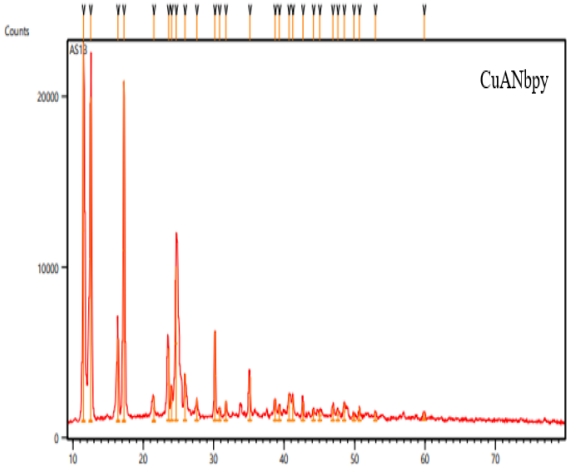

FIGURE 15 The XRD pattern of CuANbpy

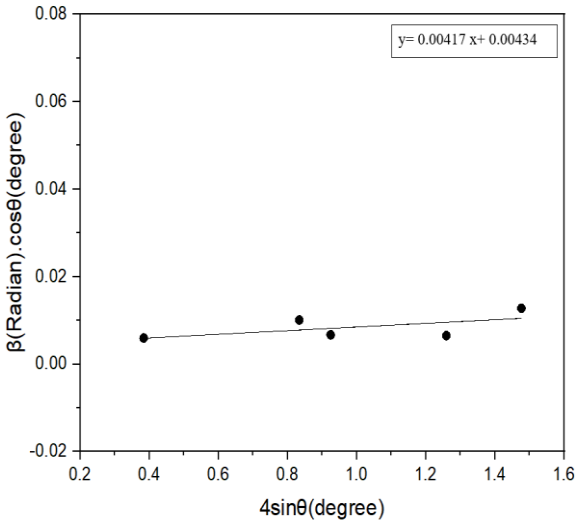

FIGURE 16 Williamson-Hall plot of the complex CuAN-Cl

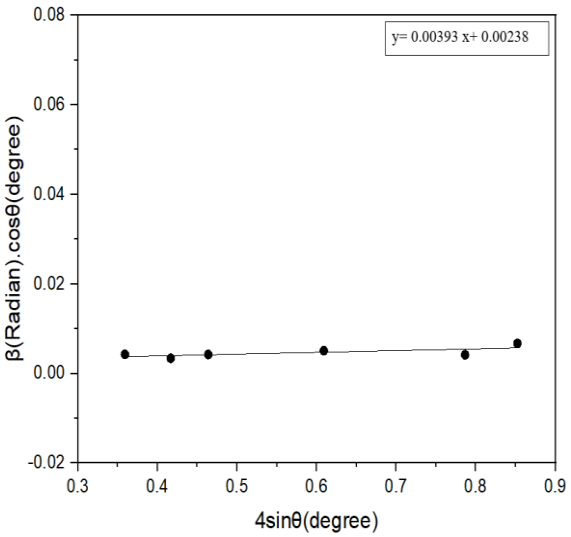

FIGURE 17 Williamson-Hall plot of the complex CuAN-Cl(bpy)

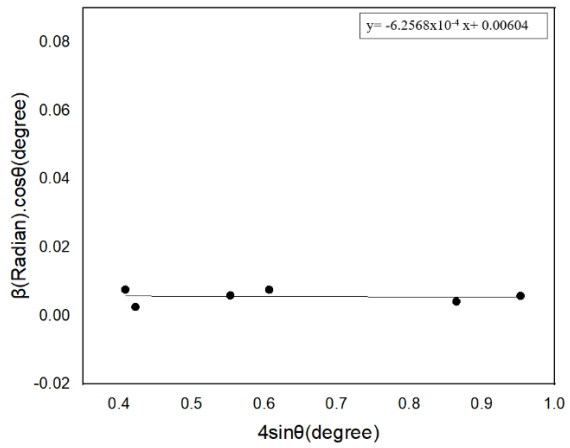

FIGURE 18 Williamson-Hall plot of the complex CuAN

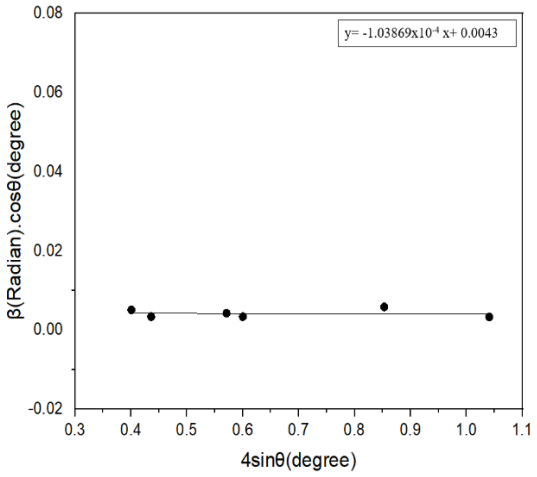

FIGURE 19 Williamson-Hall plot of the complex CuAN(bpy)

TABLE 2 Crystal size and strain of complexes from Scherrer and Williamson-Hall equations

Complexes	Crystal size Dp		ε(Strain)
	Scherrer equation	Williamson-Hall equation	
CuAN-Cl	18.76	33.37	0.00417
CuAN-Cl(bpy)	29.80	60.85	0.00393
CuAN	28.40	23.98	-6.2568×10^{-4}
CuAN(bpy)	35	33.68	-1.03869×10^{-4}

Thermal analyses of ligands and their complexes

The thermal behavior of ligands and complexes was studied using thermal gravimetric analysis (TGA) that was recorded in nitrogen gas at a constant heating rate of 10 °C/min and 15 °C/min. Thermogravimetric analyses of the complexes AN, CuAN and CuAN(bpy) showed one phase of weight loss, started at 202.58 °C, 196.03 °C, and 201.87 °C and ended at 312.53 °C, 289.25 °C, and 268.49°C with weight loss of 94.75%, 88.09%, and 79.25%, respectively. This stage represents the breakdown of all the carbon chains and the destruction of all the components of the compound [22,23]. It is clear from the weight loss% that the thermal stability of these three compounds increase in the following sequence: AN< CuAN< CuAN(bpy). In other words, the stability of the ligand AN increases after formation the copper complex CuAN, and then increases notably after formation of the five-coordinated complex, i.e. via the coordination with 4,4'-bipyridine and formation of the adduct CuAN(bpy). Higher thermal stability was noted for AN-Cl compared with AN. This conclusion is based on both the increase of decomposition temperatures and the decrease in weight loss of AN-Cl. TG curve of AN-Cl consists of three losses stages with the total weight loss of 62.91%, while only one weight-loss stage of 94.75% was noted for AN. These three stages of AN-Cl weight losses are as follows: the first stage starts at 180.26 °C and ends at 199.38 °C which includes roughly the loss of two chlorine atoms and the hydroxy group. The second stage starts at 275.62 °C and ends at 372.54 °C which corresponds to the loss of ethylene diamine [24]. The third stage begins at 374.90 °C and ends at 599.15 °C and is due to the loss of carbon dioxide. Thermogravimetric analyses of the complexes CuAN-Cl and CuAN-Cl(bpy)

showed two phases of weight losses, as shown in Figures 24 and 25 and Table 3. These phases were as follows: the first stages of CuAN-Cl and the adduct complex CuAN-Cl(bpy) start at 150.14 °C and 165.77 °C and end at 166.67 °C and 197.17 °C, respectively. These first stages include the loss of two chlorine atoms for CuAN-Cl and two chlorine atoms with ethylenediamine moiety for CuAN-Cl(bpy). The second stages for CuAN-Cl and CuAN-Cl(bpy) begin at 173.49 °C and 198.74 °C and ends at 452.60 °C and 598.01°C, respectively which correspond to the losses of ethylenediamine and bipyridine group, respectively. The total weight losses for CuAN-Cl and CuAN-Cl(bpy) are 35.3% and 56.1% respectively which means the higher stability for CuAN-Cl than the adduct CuAN-Cl(bpy), in contrast to the case of CuAN and the adduct CuAN(bpy). The thermal stability increase in the sequence CuAN-Cl< AN-Cl < CuAN-Cl(bpy). Therefore, the thermal stability of all the ligands and complexes increases in the sequence: AN< CuAN< CuAN(bpy)< CuAN-Cl(bpy)< AN-Cl < CuAN-Cl, see Figures 20-25. Likewise, it is clear that the complex CuAN-Cl has interestingly the highest stability and the ligand AN has the lowest one. The AN substitution with two chlorine atoms increases the thermal stability of the ligand AN-Cl itself and its complexes CuAN-Cl and CuAN-Cl(bpy) compared with copper complexes of AN.

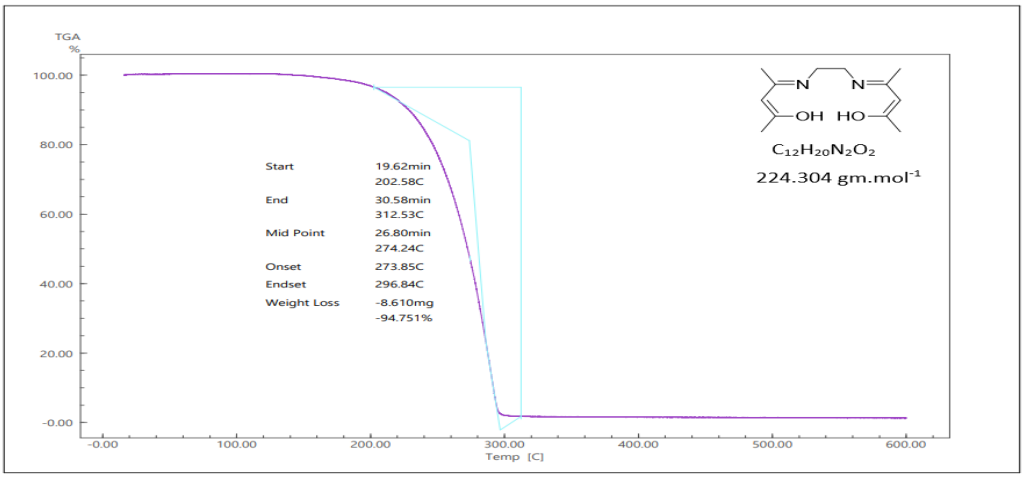

FIGURE 20 Thermal gravimetric analysis curve of AN

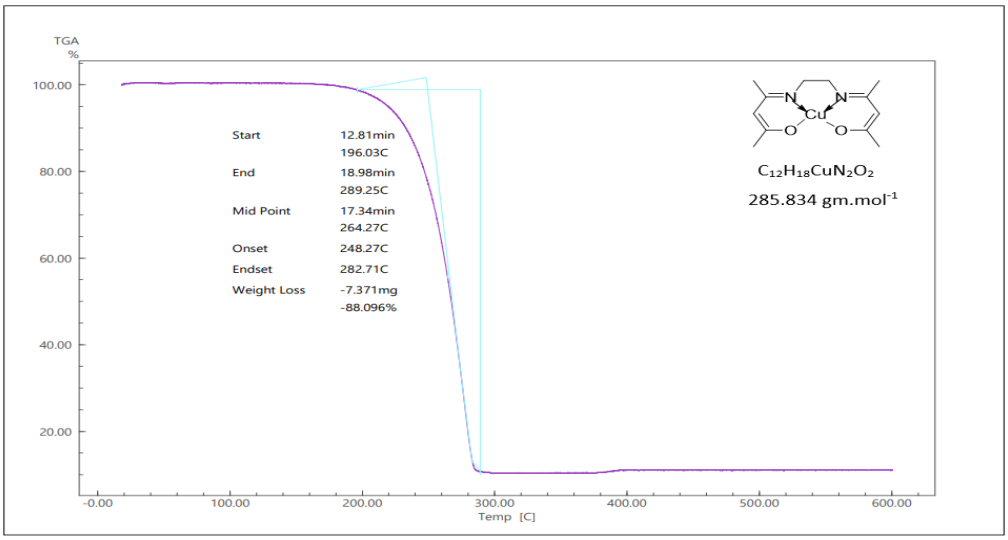

FIGURE 21 Thermal gravimetric analysis curve of CuAN

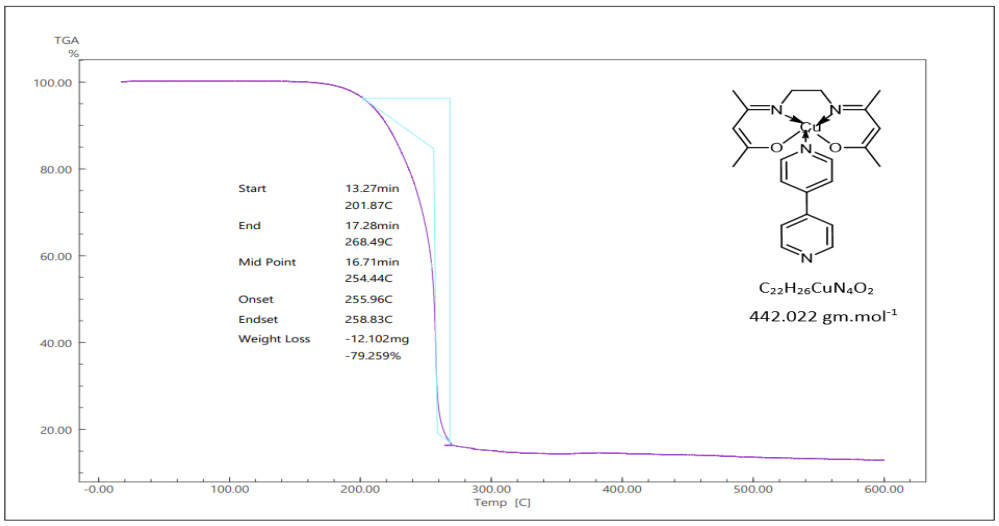

FIGURE 22 Thermal gravimetric analysis curve of CuANbpy

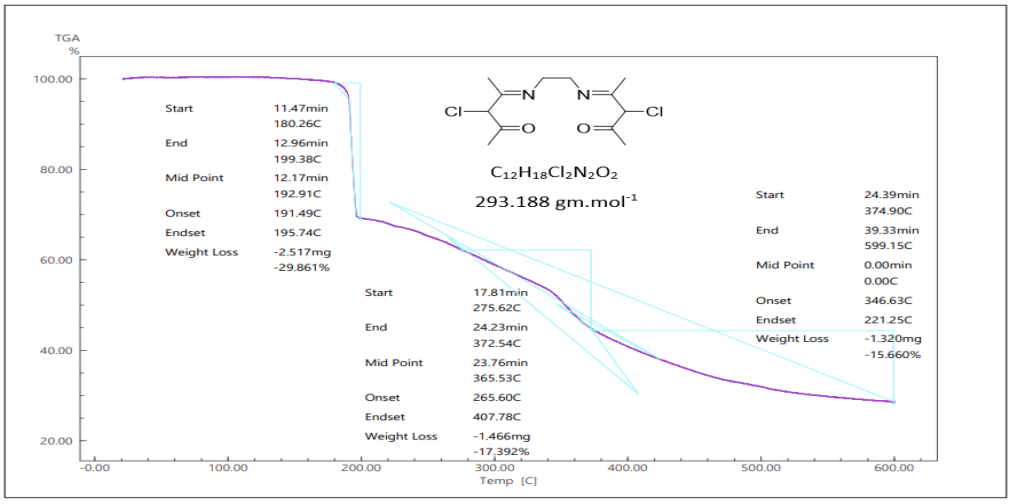

FIGURE 23 Thermal gravimetric analysis curve of AN-Cl

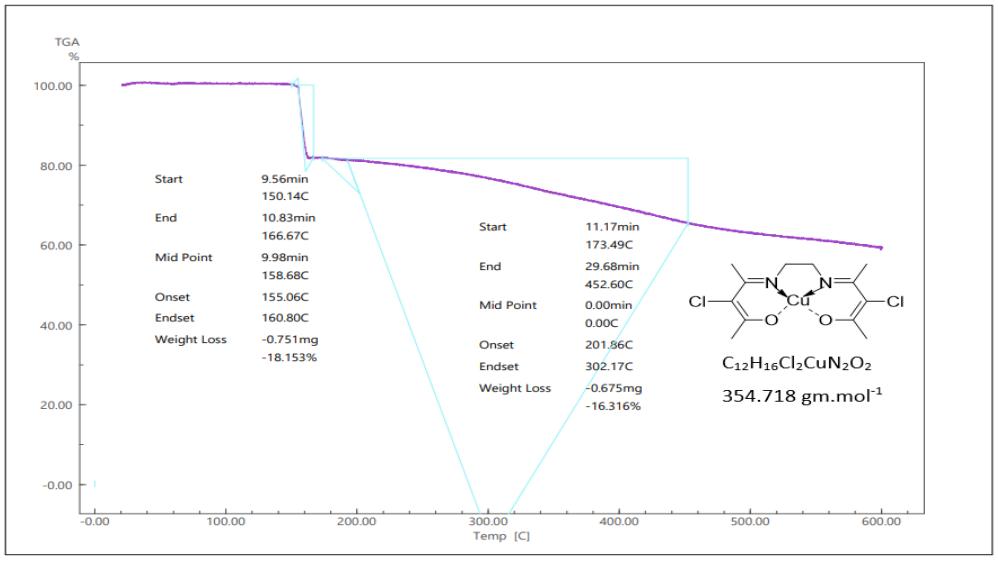

FIGURE 24 Thermal gravimetric analysis curve of CuAN-Cl

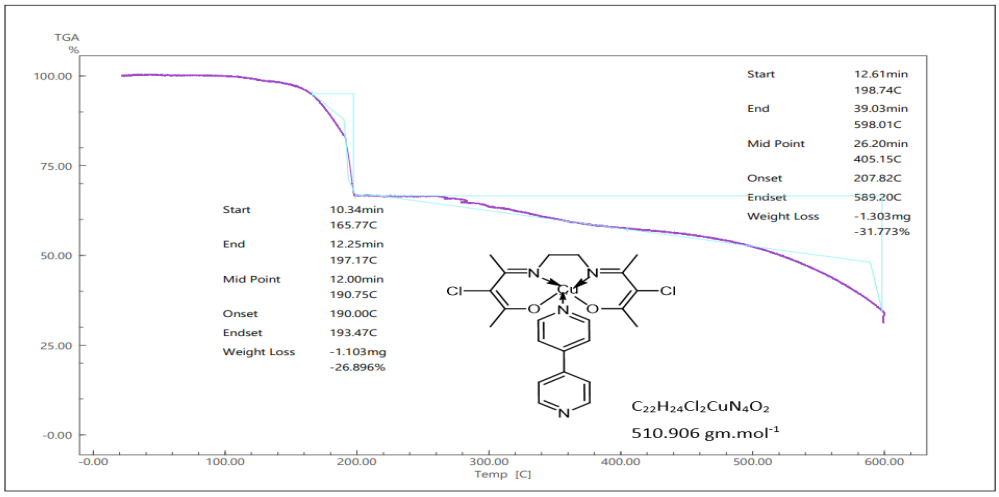

FIGURE 25 Thermal gravimetric analysis curve of CuAN-Cl(bpy)

TABLE 3 Thermal analyses data of ligands and their complexes

Complex	Temperature range (°C)	Weight loss %		Decomposition product
		Found	Calculated	
AN	202.58- 312.53	94.6	94.75	Decomposition of the compound
CuAN	196.03- 289.25	88.7	88.09	Decomposition of the compound
CuAN(bpy)	201.87-268.49	79.28	79.25	Decomposition of the compound
AN-Cl	180.26- 199.38	29.9	29.86	2Cl + OH
	275.62- 372.54	19.1	17.39	NCH_2CH_2N
	374.90- 599.15	15	15.66	CO_2
CuAN-Cl	150.14- 166.67	19	18.15	2Cl
	173.49, 452.60	16.3	16.31	$NH_2CH_2CH_2NH_2$
CuAN-Cl (bpy)	165.77, 197.17	25.6	26.89	$2Cl + NH_2CH_2CH_2NH_2$
	198.74, 598.01	30.5	31.77	Bpy

UV-Visible absorption spectroscopy of ligands and Cu (II) complexes

The UV-Visible absorption spectra of CuAN-Cl and copper acetate are recorded in acetonitrile, as displayed in Figure 26. In the UV region, two bands: an intense band at 298 nm and a weak band at 372 nm are noted for copper acetate which can be assigned to the allowed π-π* transition. While, the three π-π* transition bands of CuAN-Cl occurred at higher energies: 232 nm, 268 nm, and 324 nm. The copper acetate showed one broad d-d transition [34] band at 670 nm. At lower energy, the CuAN-Cl showed three d-d transition [25] bands at 404 nm, 547 nm, and 632 nm which are originally composed of three transitions $^2b_1g \rightarrow {}^2b_2g$, $^2b_1g \rightarrow {}^2a_1g$, and $^2b_1g \rightarrow {}^2eg$. Accordingly, the complex CuAN-Cl could adopt the square planar geometry [26]. Despite of the possible interaction between ACN solvent and the acetate ion within copper acetate, the blue shift of d-d transition (632 nm) of the CuAN-Cl compared with that of copper acetate (679 nm) supports the formation of the complex CuAN-Cl, as presented in Table 4.

The UV-Visible absorption spectra of ligands: AN and AN-Cl, their complexes: CuAN, CuAN-Cl, and adducts: CuANbpy and CuAN-Clbpy, respectively, are recorded in different solvents, as shown in Figures 27-38.

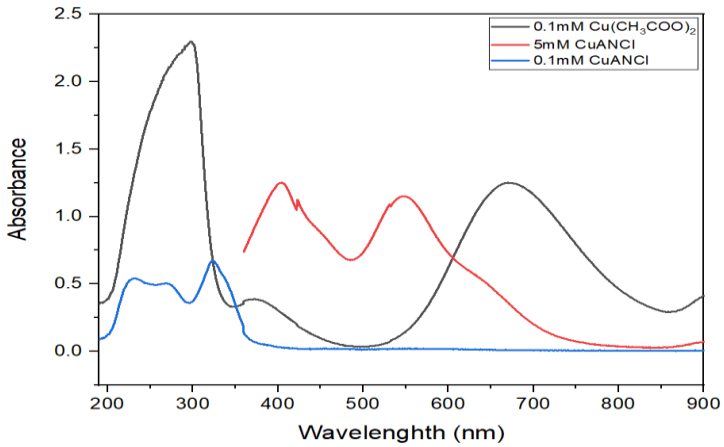

FIGURE 26 The UV-visible absorption spectra of 0.1 mM Cu $(CH_3COO)_2$ and both 0.1 mM and 5 mM CuAN-Cl in ACN at r.t. using quartz cell with a path length of 1 cm

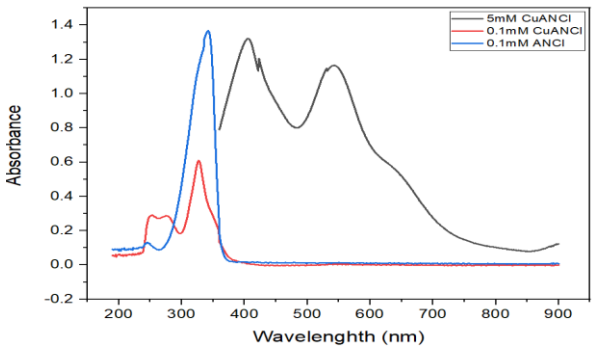

FIGURE 27 The UV-visible absorption spectra of 0.1 mM AN-Cl and both 0.1 mM and 5 mM CuAN-Cl in $CHCl_3$ r.t. using quartz cell with a path length of 1 cm

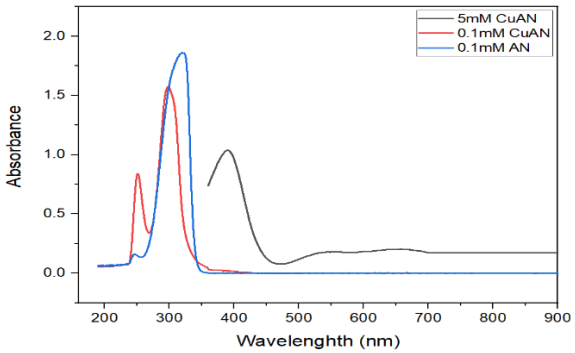

FIGURE 28 The UV-visible absorption spectra of 0.1 mM AN and both 0.1 mM and 5 mM CuAN in $CHCl_3$ r.t. using quartz cell with a path length of 1 cm

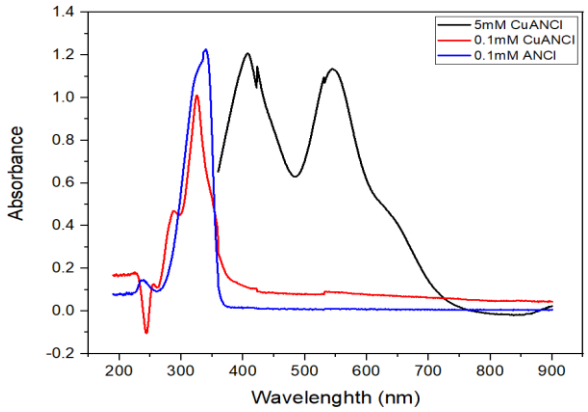

FIGURE 29 The UV-visible absorption spectra of 0.1 mM AN-Cl and both 0.1 mM and 5 mM CuAN-Cl in DCM r.t. using quartz cell with a path length of 1 cm

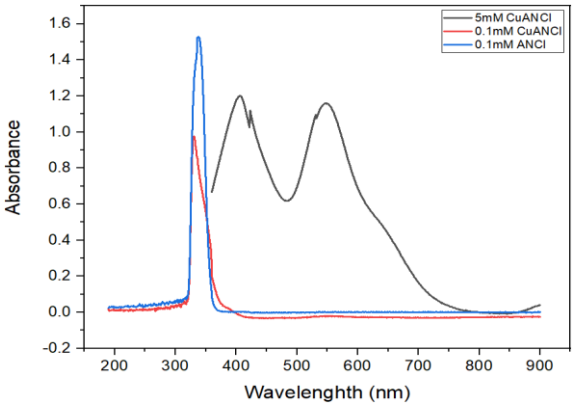

FIGURE 30 The UV-visible absorption spectra of 0.1 mM AN-Cl and both 0.1 mM and 5 mM CuAN-Cl in acetone r.t. using quartz cell with a path length of 1 cm

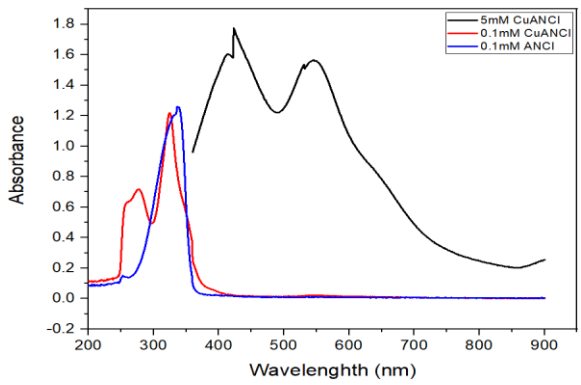

FIGURE 31 The UV-visible absorption spectra of 0.1 mM AN-Cl and both 0.1 mM and 5 mM CuAN-Cl in EtOAc r.t. using quartz cell with a path length of 1 cm

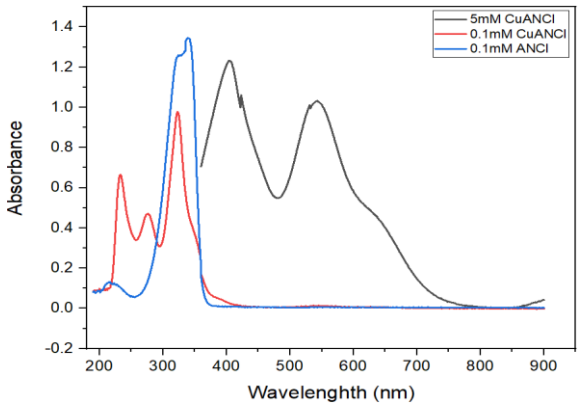

FIGURE 32 The UV-visible absorption spectra of 0.1 mM AN-Cl and both 0.1 mM and 5 mM CuAN-Cl in EtOH r.t. using quartz cell with a path length of 1 cm

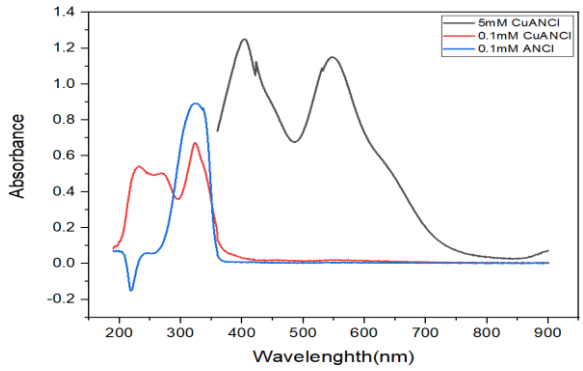

FIGURE 33 The UV-visible absorption spectra of 0.1 mM AN-Cl and both 0.1 mM and 5 mM CuAN-Cl in ACN r.t. using quartz cell with a path length of 1 cm

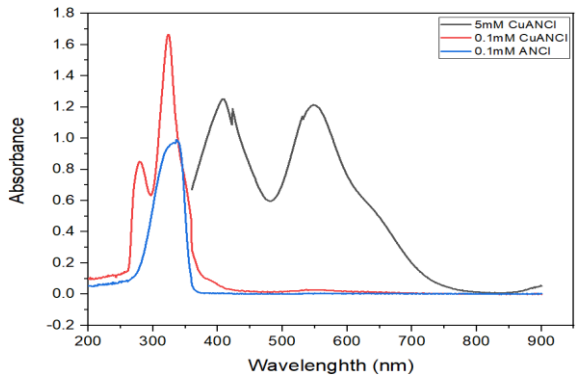

FIGURE 34 The UV-visible absorption spectra of 0.1 mM AN-Cl and both 0.1 mM and 5 mM CuAN-Cl in DMF r.t. using quartz cell with a path length of 1 cm

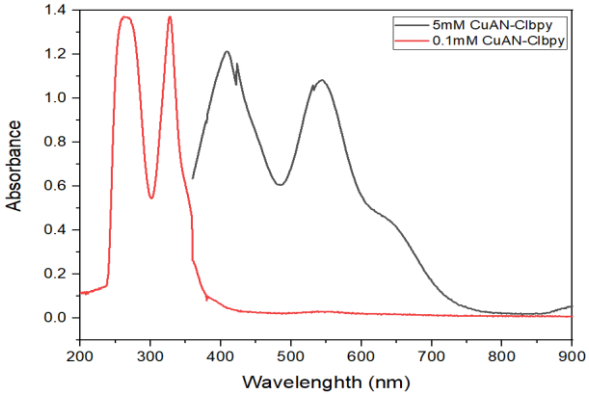

FIGURE 35 The UV-visible absorption spectra of 0.1 mM and 5 mM CuAN-Cl(bpy) in $CHCl_3$ r.t. using quartz cell with a path length of 1 cm

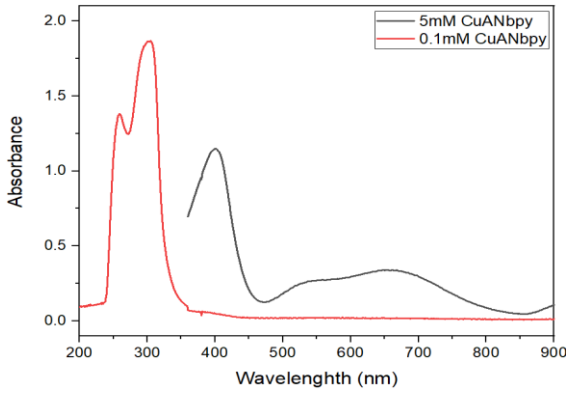

FIGURE 36 The UV-visible absorption spectra of 0.1 mM and 5 mM CuAN(bpy) in $CHCl_3$ r.t. using quartz cell with a path length of 1 cm

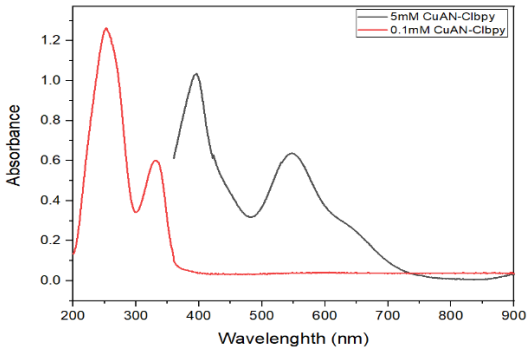

FIGURE 37 The UV-visible absorption spectra 0.1 mM and 5 mM CuAN-Cl(bpy) in ACN r.t. using quartz cell with a path length of 1 cm

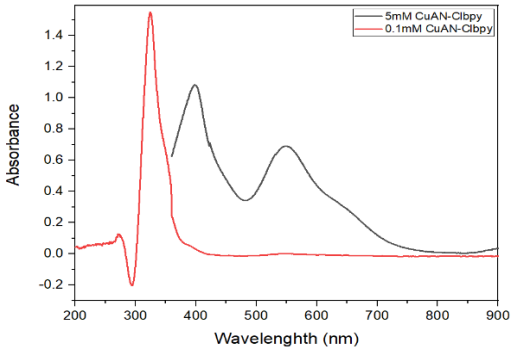

FIGURE 38 The UV-visible absorption spectra of 0.1 mM and 5 mM CuAN-Cl(bpy) in DMF r.t. using quartz cell with a path length of 1 cm

TABLE 4 The maximum wavelengths and molar absorption coefficients for 0.1 mM $Cu(CH_3COO)_2$, AN-Cl, AN, and both 5 mM and 0.1 mM CuAN-Cl, CuAN complexes

Compound	λ_{max} / nm (Ɛ. $M^{-1}.cm^{-1}$)	Solvent
0.1 mM AN	245 (6160), 320 (18620)	
0.1 mM CuAN	251(8470), 297 (15760)	
5 mM CuAN	391 (208), 535 (35), and 649 (41)	
0.1 mM CuAN(bpy)	259 (13810), 305 (18670)	$CHCl_3$
5 mM CuAN(bpy)	401 (230), 531 (51), and 648 (68)	
0.1 mM AN-Cl	245 (1310), 342 (13680)	
0.1 mM CuAN-Cl	254 (2910), 275 (2880), and 327 (6090)	
5 mM CuAN-Cl	406 (264.2), 543 (233), and 639 (112.4)	
0.1 mM CuAN-Cl(bpy)	263 (13720), 328 (13720)	
5 mM CuAN-Cl(bpy)	409 (243), 544 (217), and 642 (88)	
0.1 mM AN-Cl	236 (1410), 340 (12270)	DCM
0.1 mM CuAN-Cl	287 (4690), 325 (10100)	
5 mM CuAN-Cl	408 (242), 545 (227), and 632 (95)	
0.1 mM AN-Cl	337 (15280)	
0.1 mM CuAN-Cl	331 (9760)	Acetone
5 mM CuAN-Cl	406 (240), 546 (232), and 638 (99)	
0.1 mM AN-Cl	252 (1450), 337 (12590)	
0.1 mM CuAN-Cl	258 (6260), 278 (7180), and 325 (12190)	EtOAc
5 mM CuAN-Cl	408 (355), 545 (313), 637(171)	
0.1 mM AN-Cl	215 (1320), 339 (13460)	
0.1 mM CuAN-Cl	233 (6650), 277 (4710), and 323 (9780)	EtOH
5 mM CuAN-Cl	405 (246), 543 (206), and 637 (91)	
0.1 mM AN-Cl	325 (89300)	
0.1 mM CuAN-Cl	232 (5430), 268 (5050), and 324 (6730)	
5 mM CuAN-Cl	404 (250), 547 (230), and 632 (113)	ACN
0.1 mM CuAN-Cl(bpy)	253 (12630), 331 (6010)	
5 mM CuAN-Cl(bpy)	399 (207), 548 (128), and 633(57)	
0.1 mM Cu $(CH_3COO)_2$	298 (22980), 372 (3870), and 670 (12510)	
0.1 mM AN-Cl	325 (8930)	
0.1 mM CuAN-Cl	279 (8490), 324 (16650)	
5 mM CuAN-Cl	404 (250), 547 (230), and 640 (109)	DMF
0.1 mM CuAN-Cl(bpy)	324 (15490)	
5 mM CuAN-Cl(bpy)	400 (217), 549 (138), and 645 (60)	

The spectra of complexes are recorded at a low concentration (0.1 mM) and a high concentration (5 mM) to note clearly absorption bands in the UV and Visible regions of the spectrum. Their electronic absorption data are listed in Table 1. In the UV region of the spectrum, two bands (a weak band at 245 nm and an intense band at 320 nm) are noted for the ligand AN in $CHCl_3$. Likewise, two transition bands are noted for the ligand AN-Cl in $CHCl_3$, weak and intense bands occurred at 245 nm and 342 nm which are, respectively, at same position and red shifted compared with those of the ligand AN. This weak band of the highest energy for AN-Cl is noted at 245 nm, 236 nm, 252 nm, and 215 nm in the solvents: $CHCl_3$, DCM, EtOAc, and EtOH, respectively. The second intense band of lowest energy for the ligand AN-Cl is blue shifted (except for EtOH) as the solvent polarity increases. It appeared at 342 nm, 340 nm, 337 nm, 337 nm, 339 nm, 325 nm, and 325 nm in $CHCl_3$, DCM, acetone, EtOAc, EtOH, CAN, and DMF, respectively. These absorption bands of both the ligands AN and AN-Cl are attributed to the coincidence between n-π* and π-π* electronic transitions within the higher hydrogen bonded structures of these two ligands. In terms of polarity, the non-bonding orbital (n) is more polar than the π* orbital in turn is more polar than the π orbital. In a more polar solvents, both π and π* orbitals get stabilized but to different extents. Because the π* orbital is more polar than the π orbital, so in a more polar solvent, the magnitude of stabilizing of π* orbital of the highest energy will be greater than the magnitude of stabilizing of π orbital of the lowest energy. Thus, in a more polar solvent, the lowering in the energy of π* orbital will be more than the lowering in the energy of π orbital. Therefore, the energy gap (ΔE) between the π and π* orbitals in a more polar solvent will be less than that in less polar solvent. Thus, λ_{max} in more polar solvent will be greater than λ_{max} in less polar solvent ($\Delta E \alpha 1/ \lambda_{max}$). There will be a bathochromic (red) shift of the π-π* absorption band in a more polar solvent. Now, let us discuss the effect of solvent polarity on the λ_{max} of n-π* transition [27]. In a more polar solvent, both n and π* orbitals get stabilized but to different extents because, n orbital is more polar than π* orbital, so in a more polar solvent, the magnitude of stabilizing of n orbital will be greater than π* orbital. Thus, in a more polar solvent, the lowering in energy of n orbital will be more than the lowering in the energy of π* orbital. Here, the energy gap between the n and π* orbitals in a more polar solvent will be greater than its value in less polar solvent. Therefore, the λ_{max} of the transition n-π* in a more polar solvent will be less than λ_{max} in less polar solvent. There will be hypsochromic (blue) shift in n-π* transition band in a more polar solvent. In our case, at increasing solvent polarity, the higher intensity π-π* transition shows the red shift, while the lower intensity n-π* transition shows blue shift. In other words, both transitions get closer from each other at increasing solvent polarity. For our ligands: AN and AN-Cl, there is a very strong hydrogen bonding among C=N and O-H groups, i.e. C=N.....OH. This is supported by their existence as 100% hydrogen bonded structure in DMSO-d_6, despite that the hydrogen bonding decrease with increase the polarity solvent. The hydrogen bonding weakens the n-π* transition and makes it suffering from blue shift. Therefore, in addition to above-mentioned reasons, the strong hydrogen bonding in these ligands makes the position of n-π* transition get closer to π-π* transition. Thus, the π-π* transition of the higher intensity is merged with the n-π* transition of the lowest intensity in the ligands AN and AN-Cl. The UV-absorption spectrum of CuA complex in $CHCl_3$ showed two intense absorption bands at 251 nm and 297 nm which are red and blue shifted, respectively, compared with those of the ligand AN. In the same way, the highest energy band (245 nm) of AN-Cl in $CHCl_3$ is noted at lower energy (254 nm and 275 nm) for the

complex CuAN-Cl, while the lowest energy band (342 nm) of AN-Cl is blue shifted in the complex CuAN-Cl to be at 327 nm. The highest energy band for AN-Cl occurred at 236 nm, 252 nm, and 215 nm in DCM, EtOAc, and EtOH, respectively are red shifted and noted as absent in DCM, two intense bands at 258 nm and 278 nm in EtOAc and two intense bands at 233 nm and 277 nm in EtOH. The lowest energy bands of AN-Cl (with the highest intensities) that occurred at 340 nm, 337 nm, 337 nm, 339 nm, 325 nm, and 325 nm are also blue shifted for CuAN-Cl and noted at 287 nm and 325 nm in DCM, 331 nm in Acetone, 325 nm in EtOAc, 323 nm in EtOH, 324 nm in ACN and 324 nm in DMF, respectively. The differences in positions and intensities of the UV absorption bands compared with those of the ligands support the formation of copper (II) complexes that have more planarities than their ligands. In the Visible region of the spectrum, CuAN in $CHCl_3$ and CuAN-Cl in different solvent showed three bands due to the d-d transitions within the coordinated copper (II) ion. These transitions are attributed to $^2b_1g \rightarrow {}^2b_2g$, $^2b_1g \rightarrow {}^2a_1g$, and $^2b_1g \rightarrow {}^2eg$ which are consistent with square planer geometry [28]. The color differences of copper (II) complexes solutions compared with those of ligands and metal ions before mixing could be preliminary evidence of the occurrence of the coordination between copper (II) ion and the ligands [29]. The reaction of CuAN and CuAN-Cl with 4,4'-bipyridine at lab. temperature afforded adducts: the greenish blue crystalline CuANbpy and the dark green crystalline CuAN-Clbpy, respectively. Like the precursor: CuAN, the adduct CuANbpy is soluble in $CHCl_3$ only. While, the adduct CuAN-Clbpy is less soluble compared with its precursor CuAN-Cl. It is soluble in $CHCl_3$, CAN, and DMF. The UV absorption bands of the adducts: CuANbpy and CuAN-Clbpy are red shifted compared with those of their precursors: CuAN and CuAN-Cl, respectively [30]. Mostly, the Visible absorption bands of the adducts are red shifted with those of their precursor complexes. These absorption bands of the adducts are due to d-d transitions: $^2b_1 \rightarrow {}^2b_2$, $^2b_1 \rightarrow {}^2a_1$, and $^2b_1 \rightarrow {}^2e$, 401 nm, 537 nm, and 648 nm in $CHCl_3$ for CuANbpy, 409 nm, 544 nm, and 642 nm in $CHCl_3$, 399 nm, 548 nm, and 633 nm in ACN and 400 nm, 549 nm, and 645 nm in DMF for CuAN-Clbpy within the coordinated copper (II) ion.

Adducts formation among copper (II) complexes and nitrogen ligands

Adducts formation among CuAN and CuAN-Cl and 4,4'-bipyridine in $CHCl_3$

The interaction of CuAN (in $CHCl_3$) and CuAN-Cl (at two concentrations, low at 0.1 mM and high at 5 Mm) as acceptors in both $CHCl_3$ and DMF with 1 eq and 2 eq bipyridine as donor are followed by UV- and Visible absorption spectroscopy. These low and high concentrations of solutions are performed to note clearly the electronic transitions in the UV-Visible regions of spectrum, respectively. The absorption spectra are depicted in Figures 39-48. The electronic absorption data are listed in Table 5.

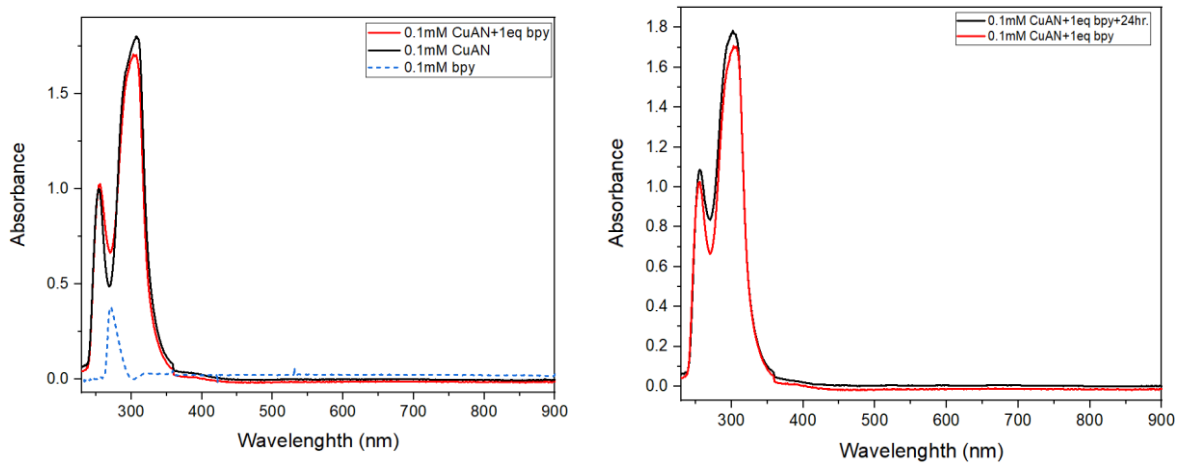

FIGURE 39 The UV-Visible absorption spectra of 0.1 mM bpy and 0.1 mM CuAN: blue and black lines in A, respectively, mixtures of 0.1 mM CuAN and 1 eq bpy: red line in A and B, and mixture of 0.1 mM CuAN and 1 eq bpy (black line in B) in $CHCl_3$ after 24 hours at r.t. using quartz cell with a path length of 1 cm

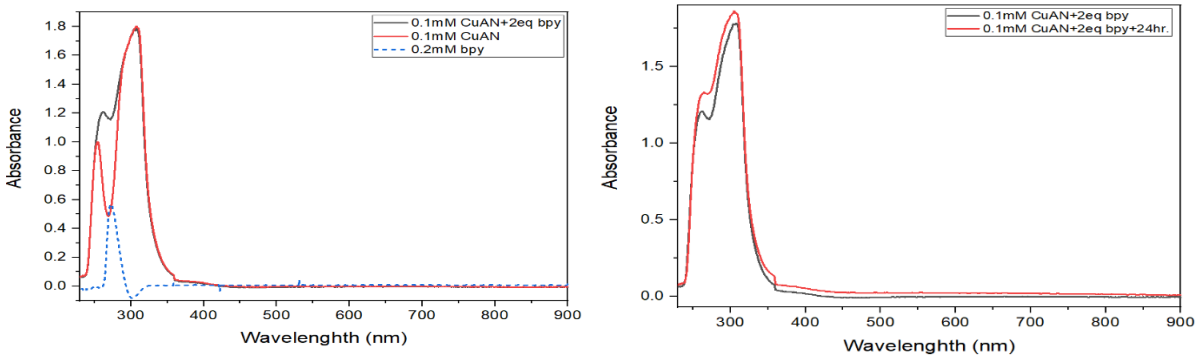

FIGURE 40 The UV-Visible absorption spectra of 0.2 mM bpy and 0.1 mM CuAN: blue and red lines in A, respectively, mixtures of 0.1 mM CuAN and 2 eq bpy: black line in A and B, and mixture of 0.1 mM CuAN and 2 eq bpy (red line in B) in $CHCl_3$ after 24 hours at r.t. using quartz cell with a path length of 1 cm

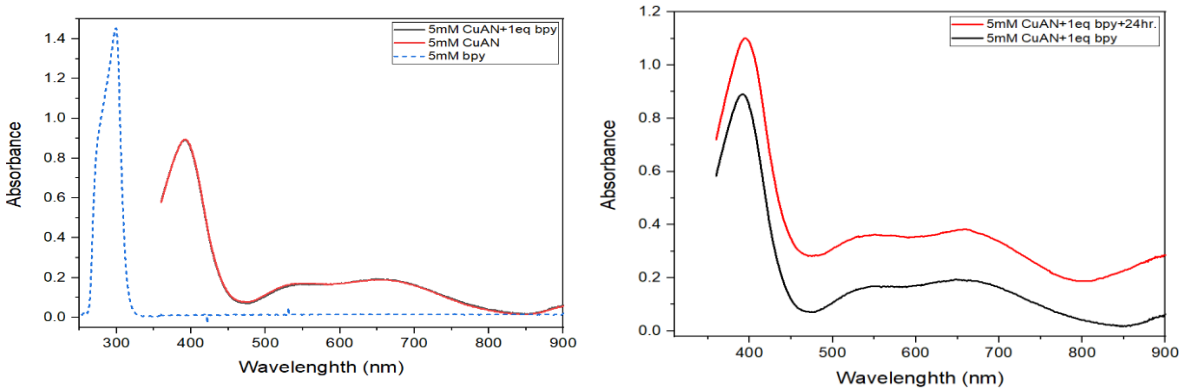

FIGURE 42 The UV-Visible absorption spectra of 5 mM bpy and 5 mM CuAN: blue and red lines in A, respectively, mixtures of 5 mM CuAN with 1 eq bpy: black lines in A and B, and mixture of 0.1 mM CuAN with 1 eq bpy (red line in B) in $CHCl_3$ after 24 hours at r.t. using quartz cell with a path length of 1 cm

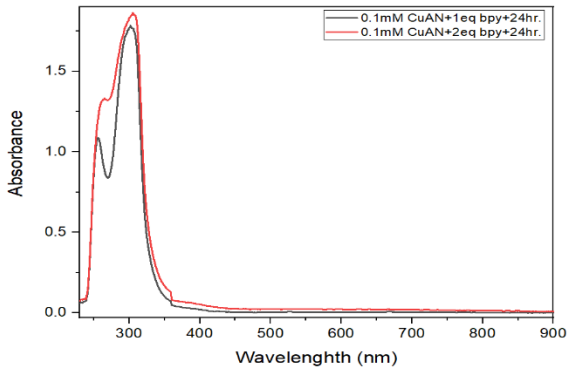

FIGURE 41 The UV-Visible absorption spectra for mixtures of 0.1 mM CuAN with 1eq and 2eq bpy after 24 hours: black and red lines, respectively in $CHCl_3$ at r.t. using quartz cell with a path length of 1 cm

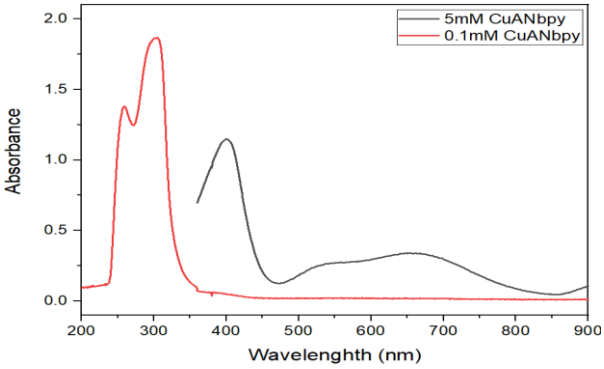

FIGURE 43 The UV-visible absorption spectra of 0.1 mM and 5 mM CuAN(bpy) in $CHCl_3$ r.t. using quartz cell with a path length of 1 cm

The absorption spectrum of 0.1 mM CuAN in $CHCl_3$ showed two intense bands at 254 nm and 307 nm (Figure 39). The peak of CuAN complex occurred at 254 nm is red shifted to 256 nm and 262 nm (more red shift) after adding 1 eq (Figure 39) or 2 eq (Figure 40) of bipyridine, respectively. After 24 hours, both two peaks of mixture of 0.1 mM CuAN with 2eq showed blue shifts to occur at 260 nm and 305 nm (Figure 40), respectively, and this is constituent with the spectrum of the synthesized adduct, CuANbpy, as depicted in Figure 43.

At the high concentration, 5 mM CuAN showed the bands: 393 nm, 536 nm, and 652 nm which after addition of 1 eq of bpy are shifted to 392 nm, 537 nm, and 648 nm, respectively. After 24 hours, these bands are more shifted to occur at 390 nm, 532 nm, and 652 nm, respectively with higher intensities. While, 5 mM solution of the synthesized CuANbpy absorbs at 401 nm, 531 nm, and 648 nm. After comparison with the synthesized CuANbpy, it is clear that the noted differences after addition 1eq or 2 eq bpy to the low or high concentration of CuAN solutions are due to the complexation of Cu(II) ion to bpy moiety affording the adduct compound CuANbpy in solution. At the lower energy side of the spectrum, an isosbestic point appeared in both bsorption spectrum of 0.1 mM CuAN-Cl and its mixture with 1 eq (see Figure 44) or with 2 eq bpy (see Figure 45). Furthermore, an isosbestic point is noted in the absorption spectra of 5 mM CuAN-Cl and its mixture with 1 eq of bpy (see Figure 47). This noted isosbestic point indicates undoubtedly to the existence of two species in equilibrium in $CHCl_3$ which are the complex: CuAN-Cl and its adduct CuAN-Clbpy.

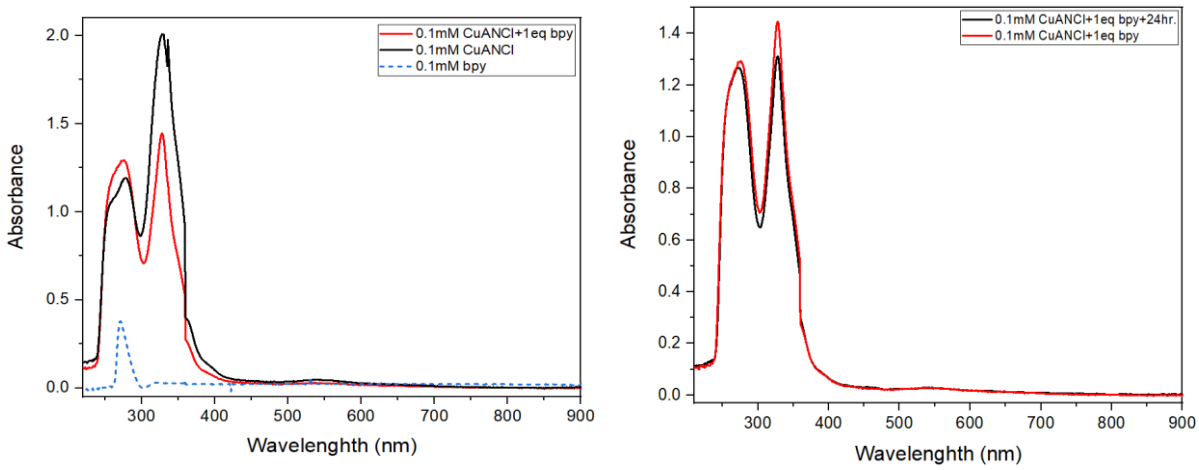

FIGURE 44 The UV-Visible absorption spectra of 0.1mM bpy and 0.1 mM CuAN-Cl: blue and black lines in A, respectively, mixtures of 0.1 mM CuAN-Cl and 1eq bpy: red line in A and B, and mixture of 0.1 mM CuAN-Cl and 1eq bpy (black line in B) in $CHCl_3$ after 24 hours at r.t. using quartz cell with a path length of 1 cm

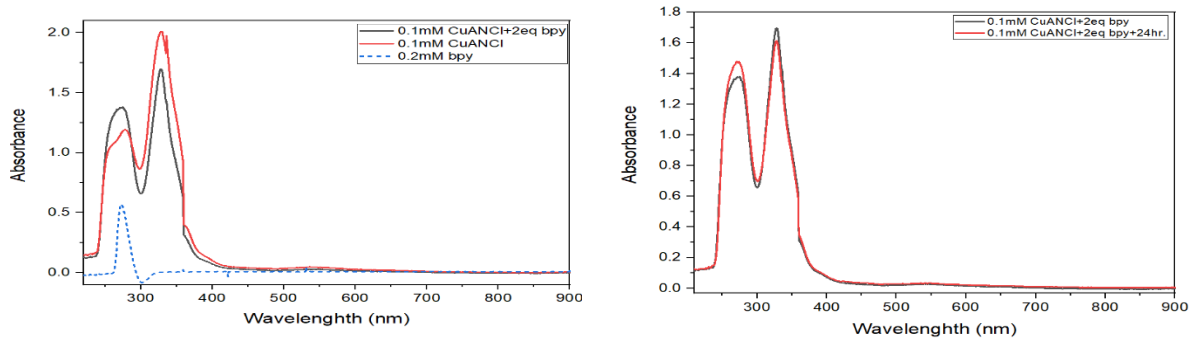

FIGURE 45 The UV-Visible absorption spectra of 0.2 mM bpy and 0.1 mM CuAN-Cl: blue and red lines in A, respectively, mixtures of 0.1 mM CuAN-Cl and 2 eq bpy: black line in A and B, and mixture of 0.1 mM CuAN-Cl and 2 eq bpy (red line in B) in $CHCl_3$ after 24 hours at r.t. using quartz cell with a path length of 1 cm

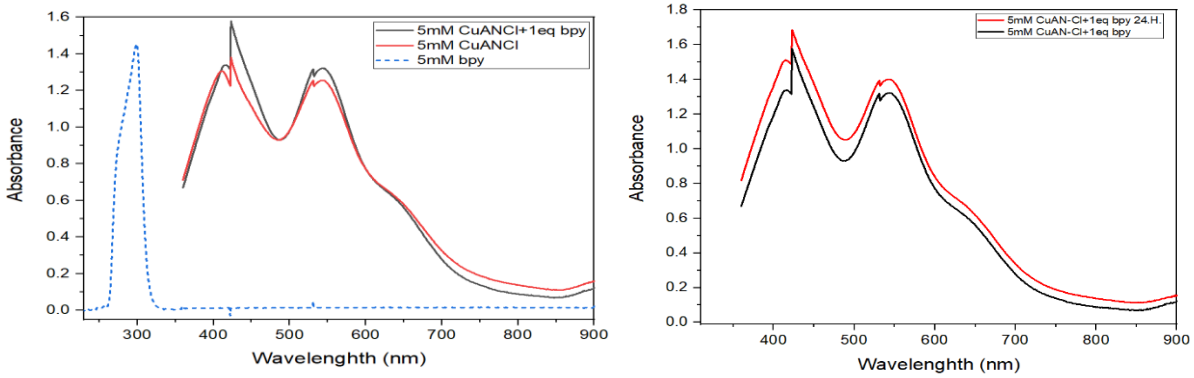

FIGURE 47 The UV-Visible absorption spectra of 5 mM bpy and 5mM CuAN-Cl: blue and red lines in A, respectively, mixtures of 5 mM CuAN and 1eq bpy: black line in A and B, and mixture of 0.1 mM CuAN and 1 eq bpy (red line in B) in $CHCl_3$ after 24 hours at r.t. using quartz cell with a path length of 1 cm

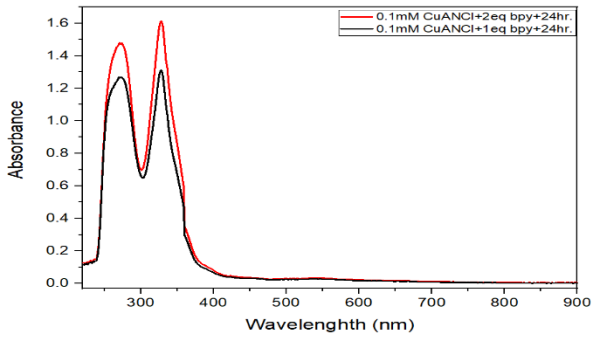

FIGURE 46 The UV-Visible absorption spectra for mixtures of 0.1 mM CuAN-Cl with 1eq and 2 eq bpy after 24 hours: black and red lines, respectively in $CHCl_3$ at r.t. using quartz cell with a path length of 1 cm

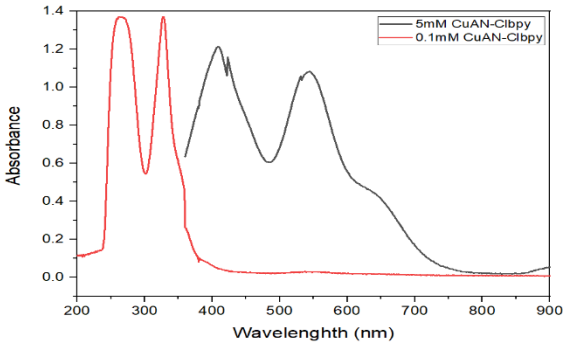

FIGURE 48 The UV-visible absorption spectra of 0.1 mM and 5 mM CuAN-Cl(bpy) in $CHCl_3$ r.t. using quartz cell with a path length of 1 cm

Three bands at 278 nm (with shoulder at highest energy), 328 nm and 357 nm are noted for 0.1 mM CuAN-Cl (see Figure 44). These bands are occurred, respectively, at 276 nm (blue shift) (absent of the shoulder), 328 nm with lower intensity and absent at addition of 1eq of bpy. The same absorption spectrum is noted after 24 hours for mixture of 0.1 mM CuAN-Cl with 1eq or 2 eq bpy. While, 5 mM CuAN-Cl absorbs at 405 nm, 423 nm, 531 nm, 543 nm, and 643 nm (Figure 47) which become at 415 nm (red shift), 420 nm (blue shift), 529 nm (blue shift), 544 nm (red shift), and 643 nm (the same) (Figure 47) after addition of 1eq of bpy. These last bands are consistent (except that at 544 nm) with the spectrum of 5 mM of the synthesized adduct CuAN-Clbpy (Figure 48) [31].

The differences in the maximum wavelengths and intensities are noted for the spectra of the mixtures of CuAN-Cl with 1 eq and 2 eq bpy compared with those of CuAN-Cl support the formation of the adduct CuAN-Clbpy in solution. The resulted spectra of these mixtures gets closer to the spectra of the synthesized adduct CuAN-Clbpy.

TABLE 5 The UV-Visible absorption data of low and high concentrations of each bpy, CuAN, and CuAN-Cl complexes and their mixtures with 1 and 2 equivalents of bpy in $CHCl_3$

Compound	λ_{max} /nm, (ε /$M^{-1}.cm^{-1}$)
0.1 mM CuAN	254 (10010), 307 (18020)
0.1 mM bpy	271(3790)
0.2 mM bpy	273 (2840)
0.1 mM CuAN+1eq bpy	256 (10260), 303 (17070)
0.1 mM CuAN+1eq bpy+ 24h.	256 (10870), 302 (17850)
0.1 mM CuAN+2eq bpy	262 (12080), 308 (17830)
0.1 mM CuAN+2eq bpy+ 24h.	260 (13060), 305 (18640)
5 mM CuAN	393 (179), 536 (34), and 652 (38)
5 mM bpy	299 (2908)
5 mM CuAN+1eq bpy	392 (178), 537 (34), and 648 (39)
5 mM CuAN+1eq bpy+24h.	390 (190), 532 (70), and 652 (40)
0.1 mM CuANbpy	259 (13810), 305 (18670)
5 mM CuANbpy	401(230), 531 (51), and 648 (68)
0.1 mM CuAN-Cl	278, (11930), 328 (20090), and 357 (9510)
0.1 mM CuAN-Cl+1eq bpy	276 (12940), 328 (14460)
0.1 mM CuAN-Cl+1eq bpy+ 24h.	270 (12680), 328 (13120)
0.1 mM CuAN-Cl+2eq bpy	275 (13810), 328 (16970), and 358 (6510)

0.1 mM CuAN-Cl+2eq bpy+ 24h.	271 (14800), 328 (16140)
5 mM CuAN-Cl	409 (261), 423 (276), 531 (251), 543 (251), and 643 (120)
5 mM CuAN-Cl+1eq bpy	415 (267), 420 (316), 529 (263), 544 (264), and 643 (119)
5 mM CuAN-Cl+1eq bpy+24h.	415 (302), 423 (337), 531 (279), 545 (280), and 643 (130)
0.1 mM CuAN-Clbpy	263 (13720), 328 (13720)
5 mM CuAN-Clbpy	409 (243), 544 (217), and 642 (88)

Adduct formation between CuAN-Cl and 4,4'-bipyridine in DMF

This study was carried out using UV-visible spectroscopy by mixing CuAN-Cl complex at 0.1 mM and 5 mM with 1 eq and 2 eq of 4,4'-bipyridine at mixing and after 24 hours from mixing in DMF, as exhibited in Figures 49-53 and Table 6.

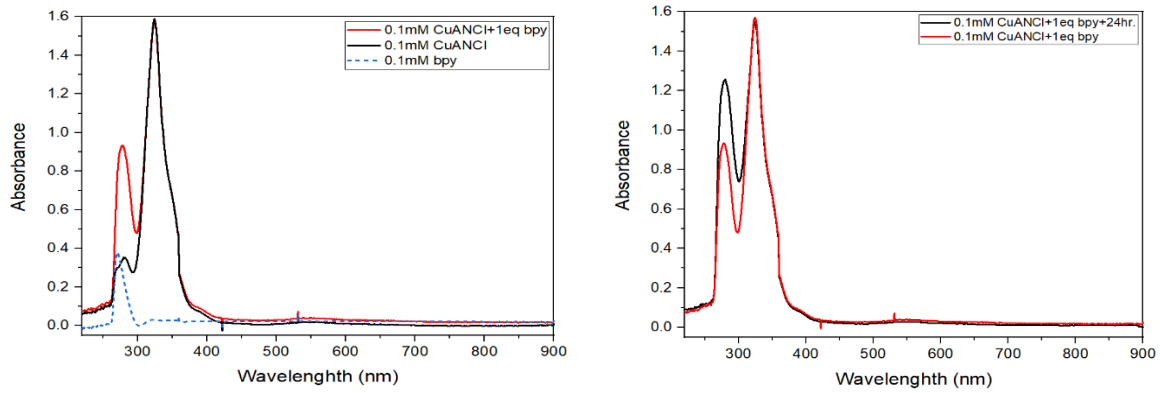

FIGURE 49 The UV-Visible absorption spectra of 0.1 mM bpy and 0.1mM CuAN-Cl: blue and black lines in A, respectively, mixtures of 0.1 mM CuAN-Cl and 1 eq bpy: red line in A and B, and mixture of 0.1 mM CuAN-Cl and 1eq bpy (black line in B) in DMF after 24 hours at r.t. using quartz cell with a path length of 1 cm

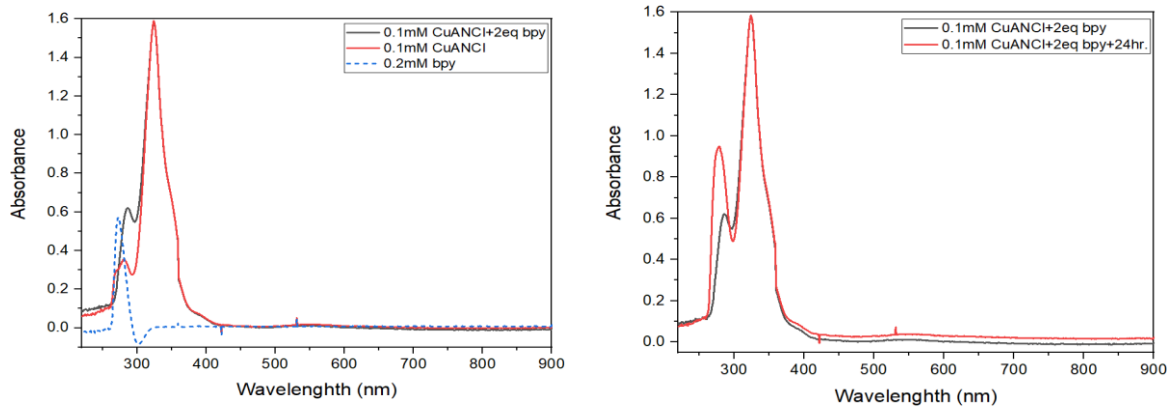

FIGURE 50 The UV-Visible absorption spectra of 0.2 mM bpy and 0.1 mM CuAN-Cl: blue and red lines in A, respectively, mixtures of 0.1 mM CuAN-Cl and 2 eq bpy: black line in A and B, and mixture of 0.1 mM CuAN-Cl and 2 eq bpy (red line in B) in DMF after 24 hours at r.t. using quartz cell with a path length of 1 cm

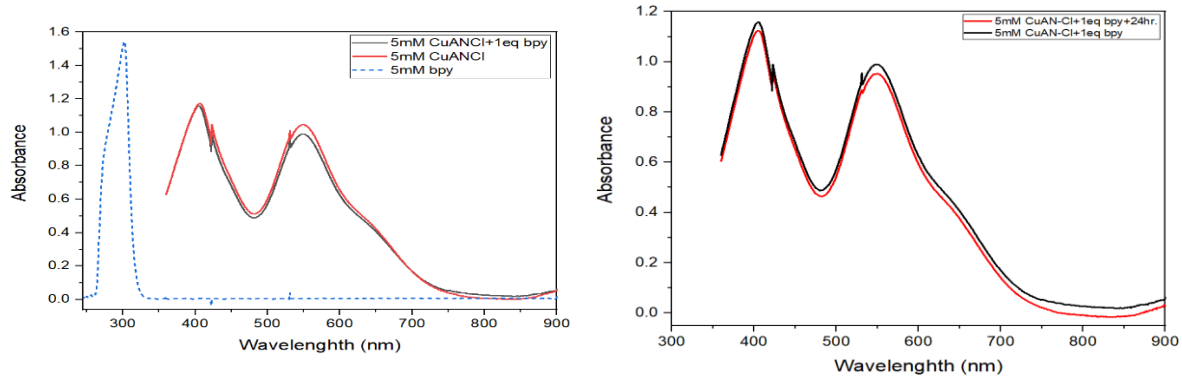

FIGURE 52 The UV-Visible absorption spectra of 5 mM bpy and 5mM CuAN-Cl: blue and red lines in A, respectively, the mixtures of 5 mM CuAN and 1eq bpy: black line in A and B, and mixture of 0.1 mM CuAN-Cl and 1eq bpy (red line in B) in DMF after 24 hours at r.t. using quartz cell with a path length of 1 cm

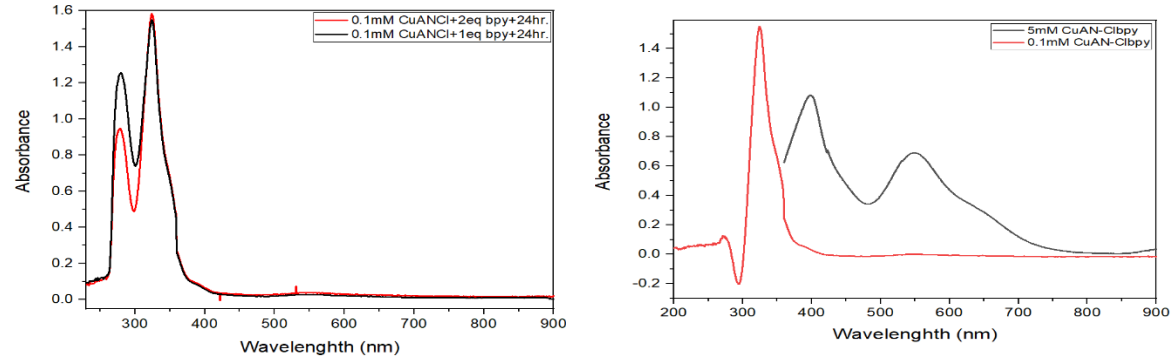

FIGURE 51 The UV-Visible absorption spectra for mixtures of 0.1 mM CuAN-Cl with 1 eq and 2 eq bpy after 24 hours: black and red lines, respectively in DMF at r.t. using quartz cell with a path length of 1 cm

FIGURE 53 The UV-visible absorption spectra of 0.1 mM and 5 mM CuAN-Cl (bpy) in DMF r.t. using quartz cell with a path length of 1 cm

The 0.1 mM CuAN-Cl solution in DMF absorbed at 280 nm, 324 nm, 356 nm, 386 nm, and 538 nm, A and B. After adding 1 eq bpy, these absorptions occurred at 278 nm (blue shift with increasing intensity), 324 nm, 356 nm, 386 nm, and 539 nm, respectively. After keeping the solution containing the resulted adduct for 24 hours to get more possible amount of adduct, only the first peak is shifted to be at 280 nm with increasing the intensity (Figure 49). With adding 2 eq of bpy instead of 1 eq bpy to the CuAN-Cl (Figure 50), the first peak is shifted to 286 nm with increasing intensity and also same peak is shifted after 24 hours from mixing to be at 279 nm with increasing intensity. It is clear that the absorption spectrum of 0.1 mM of adduct, CuAN-Clbpy is similar to spectra of mixtures of CuAN-Cl with bpy in DMF (Figure 53). [31] This supports the formation of adduct in these mixtures especially after 24 hours from the mixing.

The visible absorption spectrum of 5 mM CuAN-Cl complex showed absorptions at 407 nm, 550 nm, and 642 nm (Figure 52) which are shifted to 405 nm, 548 nm, and 643 nm after the addition of 1eq bpy in DMF. After 24 hours from mixing, almost same peaks are obtained which are normally related to use the high concentrations that afforded the formation of the maximum amount of adduct at mixing with no noted remarkable changes after 24 hours of mixing (Scheme 1).

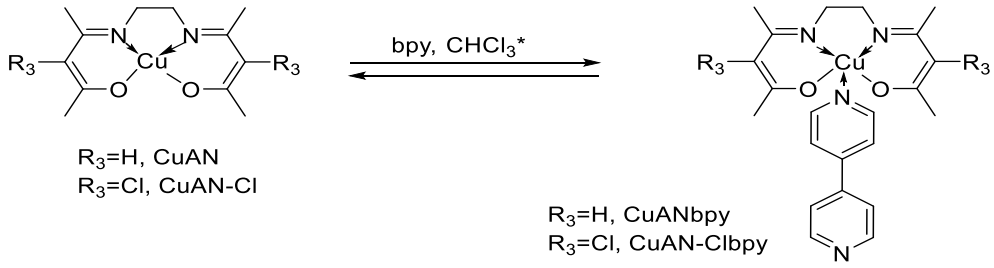

SCHEME 1 The formation of the adducts CuANbpy and CuAN-Clbpy in $CHCl_3$. * CuAN-Clbpy is also formed in DMF

Formation and reduction of the adduct CuAN-Cl. $V_2^{2+}.2PF_6^{2-}$ in DMF

The interaction of 0.1 mM and 5 mM with 1 and 2 equivalents to afford the formation of the adduct complex CuAN-Cl. $V_2^{2+}.2PF_6^{2-}$ in DMF followed by the UV-Visible absorption spectroscopy. Likewise, the resulted adduct CuAN-Cl. $V_2^{2+}.2PF_6^{2-}$ in solution was reduced to afford the dimerized viologen radicals within the adduct structures, as illustrated in Figures 54-57 and Table 6. Due to the insolubility of CuAN complex in DMF, its interaction with $V_2^{2+}.2PF_6^{2-}$ was not studied.

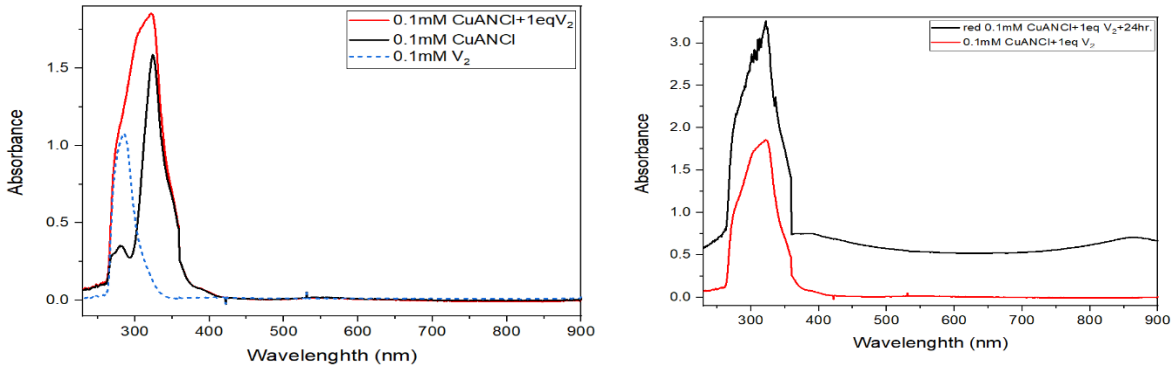

FIGURE 54 The UV-Visible absorption spectra of 0.1 mM $V_2^{2+}.2PF_6^{2-}$ and 0.1 mM CuAN-Cl: blue and black lines in A, respectively, mixtures of 0.1 mM CuAN-Cl and 1 eq of $V_2^{2+}.2PF_6^{2-}$: red line in A and B, and reduced mixture of 0.1 mM CuAN-Cl and 1eq of $V_2^{2+}.2PF_6^{2-}$ (black line in B) in DMF after 24 hours at r.t. using quartz cell with a path length of 1 cm

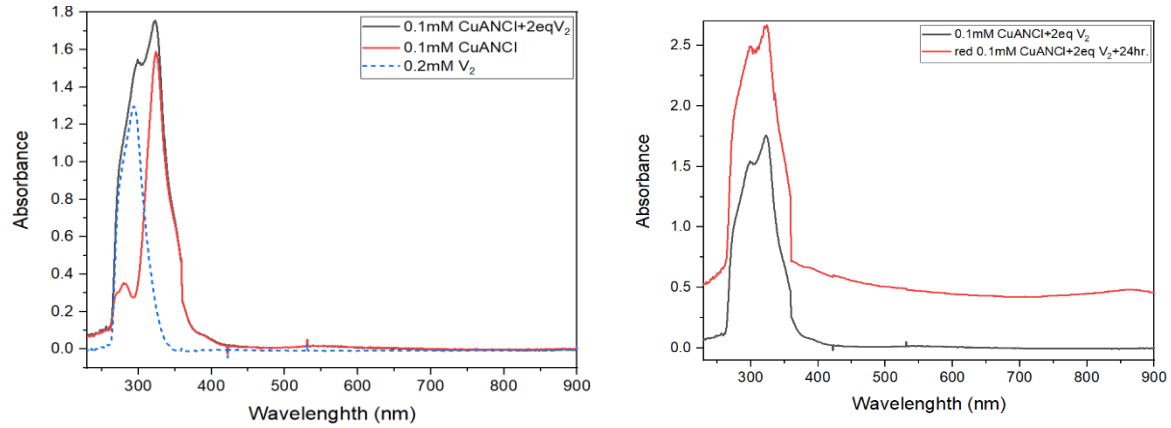

FIGURE 55 The UV-Visible absorption spectra of o.2 mM $V_2^{2+}.2PF_6^{2-}$ and 0.1 mM CuAN-Cl: blue and red lines in A, respectively, mixtures of 0.1 mM CuAN-Cl and 2eq of $V_2^{2+}.2PF_6^{2-}$: black line in A and B, and mixture of 0.1 mM CuAN-Cl and 2 eq of $V_2^{2+}.2PF_6^{2-}$ (red line in B) in DMF after 24 hours at r.t. using quartz cell with a path length of 1 cm

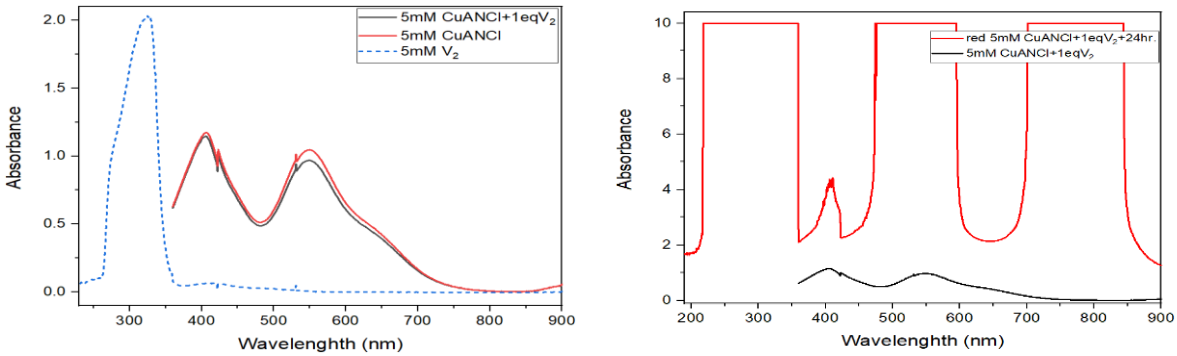

FIGURE 56 The UV-Visible absorption spectra of 5 mM $V_2^{2+}.2PF_6^{2-}$ and 5mM CuAN-Cl: blue and red lines in A, respectively, mixtures of 5 mM CuAN-Cl and 1 eq of $V_2^{2+}.2PF_6^{2-}$: black line in A and B, and mixture of 0.1 mM CuAN and 1 eq of $V_2^{2+}.2PF_6^{2-}$ (red line in B) in DMF after 24 hours at r.t. using quartz cell with a path length of 1 cm

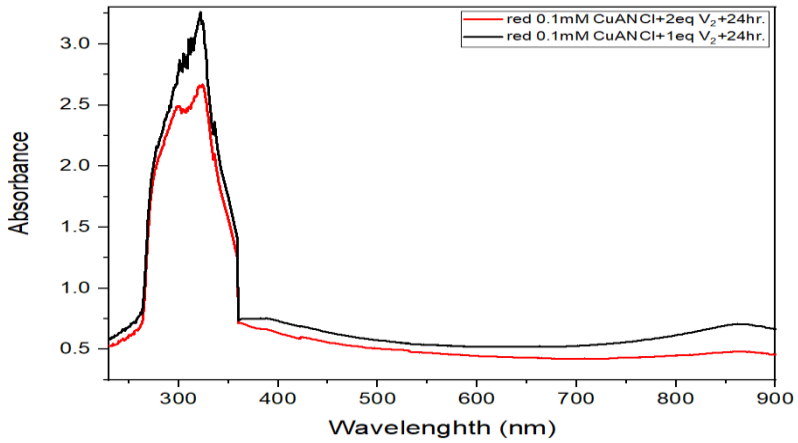

FIGURE 57 The UV-Visible absorption spectra for mixtures of 0.1 mM CuAN-Cl with 1 eq and 2 eq of $V_2^{2+}.2PF_6^{2-}$ after 24 hours: black and red lines, respectively, in DMF at r.t. using quartz cell with a path length of 1 cm

The solution of 0.1 mM CuAN-Cl in DMF absorbed at 280 nm, 324 nm, 356 nm (shoulder), 386 nm, and 538 nm. After mixing with 1eq of $V_2^{2+}.2PF_6^{2-}$, those three peaks disappeared, respectively, shifted to 322 nm (with increasing intensity), shifted to 357 nm and 384 nm.

These observed changes indicate the complexation of $V_2^{2+}.2PF_6^{2-}$ to the Cu(II) metal ion and formation of the adduct complex CuAN-Cl. $V_2^{2+}.2PF_6^{2-}$ in DMF media. The adduct complex solution has been kept at lab temperature for 24 hours after mixing to get more possible amount of the adduct complex. This adduct complex solution has been reduced by activated zinc powder and its absorption spectrum showed more intense peaks occurred at 322 nm, 358 nm with new peaks at 389 nm and 862 nm. These new peaks at 389 nm and 862 nm are correlated to the dimerized viologen radicals of $V_2^{2+}.2PF_6^{2-}$ within the structures of the adduct complex, as displayed in Figure 54, Table 6 and Scheme 2 [32].

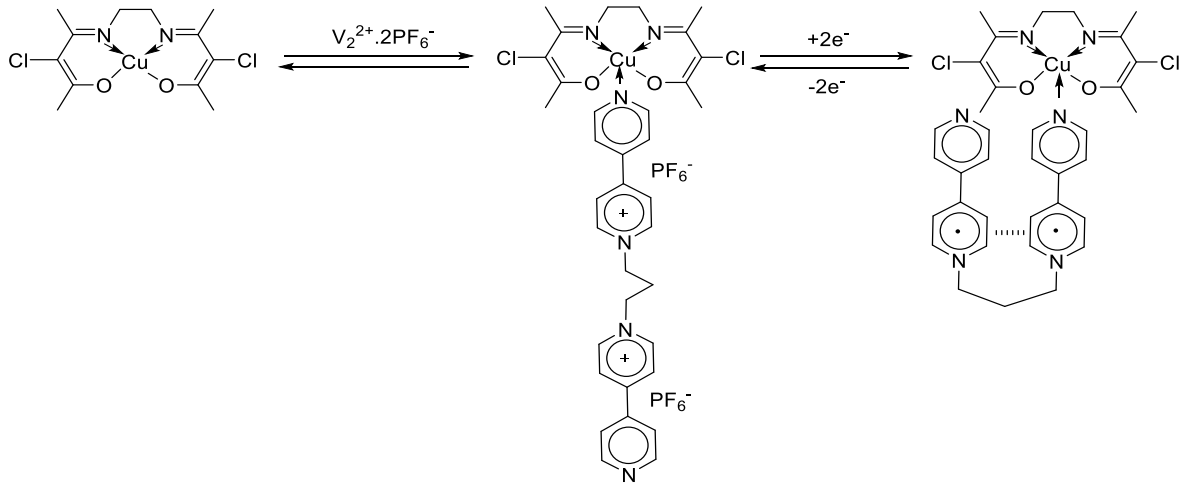

SCHEME 2 Molecular switch based on the adduct of $V_2^{2+}.2PF_6^{2-}$ and CuAN-Cl complex in DMF

With the addition of 2eq of $V_2^{2+}.2PF_6^{2-}$ to the complex CuAN-Cl instead of 1eq, and then the reduction of this mixture, almost the same previous changes are noted with lower intensities, as demonstrated in Figures 55 and 56. The visible spectrum of 5 mM CuAN-Cl showed the peaks of 407 nm, 550 nm, and 642 nm. After adding 1eq of $V_2^{2+}.2PF_6^{2-}$, those three peaks are noted at 406 nm, 548 nm, and 640 nm, respectively, with changes in their intensities. Interestingly, the reduction of the concentrated solution of the resulted adduct afforded peaks at 408 nm (with higher intensity) and two out of scale peaks occurred at less than 600 nm, and above 700 nm. These peaks are attributed, respectively, to 407 nm of adduct merged with 400 nm of viologen radicals, both of 548 nm and 640 nm of adduct merged with peak less than 600 of dimerized viologen radicals and the NIR characteristic bands above 800 nm due to the dimerized viologen radicals [33-36]. The peaks appeared at out of scale are absolutely related with the reduced higher concentration of viologen radicals coordinated to Cu (II) metal ion within the adduct structure.

TABLE 6 The UV-Visible absorption data of low and high concentrations of each bpy, $V_2^{2+}.2PF_6^{2-}$, CuAN-Cl complex, and its mixtures with 1 and 2 equivalents of bpy and $V_2^{2+}.2PF_6^{2-}$ in DMF

Compound	λ_{max} /nm, (Ɛ /$M^{-1}.cm^{-1}$)
0.1 mM bpy	270 (3780)
0.2 mM bpy	274 (2860)
0.1 mM CuAN-Cl	280 (3540), 324 (15890), 356 (5120), 386 (780), and 538 (250)
0.1 mM CuAN-Cl+1eq bpy	278 (9340), 324 (15700), 356 (5220), 386 (960), and 539 (400)
0.1 mM CuAN-Cl+1eq bpy+ 24h.	280 (12580), 324 (15490), 356 (5480), 385 (880), and 538 (270)
0.1 mM CuAN-Cl+2eq bpy	286 (6210), 324 (15760), 357 (5150), 386 (670), and 538 (120)
0.1 mM CuAN-Cl+2eq bpy+ 24h.	279 (9480), 324 (15840), 356 (5220), 386 (890), and 539 (370)
5 mM bpy	302 (309)
5 mM CuAN-Cl	407 (235), 550 (209), and 642 (92)
5 mM CuAN-Cl+1eq bpy	405 (232), 548 (198), and 643 (87)
5 mM CuAN-Cl+1eq bpy+24 h.	405 (225), 548 (190), and 643 (81)
0.1 mM CuAN-Clbpy	272 (1220), 324 (15490), and 356 (5140)
5 mM CuAN-Clbpy	400 (217), 549 (138), and 645 (60)

0.1 mM V_2	286 (10780)
0.2 mM V_2	294 (6485)
0.1 mM CuAN-Cl+1eq V_2	322 (18560), 357 (5120), and 384 (810)
Red 0.1 mM CuAN-Cl+1eq V_2+ 24 hr.	322 (32610), 358 (14660), 389 (7490), and 862 (7080)
0.1 mM CuAN-Cl+2eq V_2	323 (17560), 357 (4840)
Red 0.1 mM CuAN-Cl+2eq V_2+ 24 hr.	324 (26690), 357(13180), and 866 (4830)
5 mM V_2	273 (190), 327 (407)
5 mM CuAN-Cl	407 (235), 550 (209), and 642 (92)
5 mM CuAN-Cl+1eq V_2	406 (229), 548 (194), and 640 (86)
Red 5 mM CuAN-Cl+1eq V_2+24 hr.	408 (871)

Conclusion

The reactions of 2 equivalents of the N_2O_2 ligands AN-Cl and AN with copper (II) ion afforded the square planar CuAN-Cl and CuAN, respectively. The reactions of these two complexes with 4,4'- bipyridine at lab temperature yielded the five-coordinated adduct complexes (complexation of 4,4'-bipyridine to the complexed Cu (II). Mass spectrometry and thermal analyses supported the formation of all copper (II) complexes. The reliable differences are noted among the FT-IR spectra of the N_2O_2 ligands and those of copper (II) complexes. The XRD crystallite sizes of the five coordinated adduct complexes are bigger than those of their precursors copper (II) complexes. All N_2O_2 ligands and their complexes showed the coincidence among n-π* and π-π* electronic transitions in different solvents. The copper (II) complexes showed the expected d-d transitions. In solution, the interaction of the square plannar copper (II) complexes with axial ligands: 4,4'- bipyridine or bis-viologen and formation of five-coordinated copper (II) complexes have been proved by both UV- and Visible absorption spectroscopies. The switching motion between the five-coordinated copper complex CuAN-Cl.V_2^{2+}.2PF_6^- and the π-dimer: CuAN-Cl.V_2^{2+}.2PF_6^- (dimerization of the viologen radical of V_2^{2+}.2PF_6^-) was triggered by the reduction through two electrons in the DMF media.

Acknowledgments

The author would like to present the sincere appreciation to the supervisors, the assistant professor, Dr. Wathiq Sattar, who presented valuable information and supported throughout the research period. Also, the author would like to thank Prof. Dr. Ibrahim Abboud for his support during the research period.

Conflict of Interest

The authors declare no conflict of interest.

Orcid:

Israa A. Jassem: https://www.orcid.org/0000-0002-9609-0498

References

[1] M. Nic, J. Jirat, B. Kosata, *Schiff base. IUPAC Compendium of Chemical Terminology*, **2006**. [Crossref] [Publisher]

[2] N. Bresciani-Pahor, M. Calligaris, G. Nardin, L. Randaccio, D. Viterbo, *Acta Cryst.*, **1979**, *B35*, 2776. [Crossref], [Google Scholar], [Publisher]

[3] A.H. Gatea, S.A. Alshamkhawy, W.S. Abdul-hassan, *J. Med. Chem. Sci.*, **2022**, *5*, 743. [Crossref], [Google Scholar], [Publisher]

[4] S. Mehrpour, A. Najafi, A. Ahmadi, T. Zarei, V. Pleqi, K. Basiri, K. KomLakh, H. Abdollahi, K.H. Emami, *Frontiers in Emergency Medicine*, **2022**, *6*. [Crossref], [Google Scholar], [Publisher]

[5] P.G. Cozzi, *Chemical Society Reviews*., **2004**, *33*, 410-421. [Crossref], [Google Scholar], [Publisher]
[6] K. Masaaki, T. Hideki, T. Masanobu, N. Kiyohiko, *Coordination Chemistry Reviews.,* **2003**, *237*, 183-196. [Crossref], [Google Scholar], [Publisher]
[7] J. Costamagna, J. Vargas, R. Latorre, A. Alvarado, G. Mena, *Coordination Chemistry Reviews*, **1992**, *119*, 67. [Crossref], [Google Scholar], [Publisher]
[8] I.A. Jassem, W.S. Abdul-hassan, I.A. Flafel, S.A. Alshamkhawy, Z.M. Mahdi, *Journal of Medicinal and Chemical Sciences*, **2022**, *5*, 988. [Crossref], [Google Scholar], [Publisher]
[9] A.H. Kianfara, S. Zargarib, H.R. Khavasi, *J. Iran. Chem. Soc.*, **2010**, *7*, 908-916. [Crossref], [Google Scholar], [Publisher]
[10] A.H. Gatea, W.S. Abdul-Hassan, S.A. Ali, Z.M. Mahdi, *J. Med. Chem. Sci*., **2023**, *6*, 280-303. [Crossref], [Google Scholar], [Publisher]
[11] C. Yu-Ying, E.C. Doris, B.D. Mckinney, L.J. Willis, S.C. Cumming, *Inorg. Chem*., **1981**, *20*, 1885. [Crossref], [Google Scholar], [Publisher]
[12] A.H. Kianfar, S. Zargari, H.R. Khavasi, *J. Iran. Chem. Soc*., **2010**, *7*, 908-916. [Crossref], [Google Scholar], [Publisher]
[13] M.R. Maurya, S. Khurana, W. Zhangb, Dieter Rehder, *J. Chem. Soc., Dalton Trans*., **2002**, 3015–3023. [Crossref], [Google Scholar], [Publisher]
[14] M. Sharma, J. Tripathi, A. K. Yadav, S.N. Jha, A. Mishra, B.D. Shrivastava, *AIP Conf. Proc*., **2019**, 2115. [Crossref], [Google Scholar], [Publisher]
[15] D. Nath, F. Singh, R. Das, *Mater. Chem. Phys*., **2020**, *239*, 1220. [Crossref], [Google Scholar], [Publisher]
[16] R. Jacob, J. Isac, *Int. J. Chem. Stud*., **2015**, *2*, 12–21. [Crossref], [Google Scholar], [Publisher]
[17] N.K. Chaudhary, P. Mishra, *Bioinorganic Chemistry and Applications*, **2017**, *4*, 13. [Crossref], [Google Scholar], [Publisher]
[18] S.K. Mishra, H. Roy , A.K. Lohar , S.K. Samanta , S. Tiwari, K. Dutta: *Materials Science and Engineering*, **2015**, *75*. [Crossref], [Google Scholar], [Publisher]
[19] M. Rabiei, A. Palevicius, A. Monshi, S. Nasiri, A. Vilkauskas, G. Janusas, *Nanomaterials*, **2020**, *10*, 1627. [Crossref], [Google Scholar], [Publisher]
[20] D.S.Y. Gaëlle, D.M. Yufanyi, R. Jagan, M. O. Agwara, *Cogent Chemistry*, **2016**, *2*, 1253201. [Crossref], [Google Scholar], [Publisher]
[21] B. Sarma, D.K. Das, *Hindawi Publishing Corporation Journal of Chemistry*, **2013**, *2013*, Article ID 349580. [Crossref], [Google Scholar], [Publisher]
[22] H. Olmez, F. Arslan, H. Icbudak, *J Therm Anal Calorim*., **2004**, *76*, 793-800. [Crossref], [Google Scholar], [Publisher]
[23] K. Takeo, M. Masanori, N. Yukio, O. Shun icchiro, K. Shinichi, K. Hisao. *Bulletin of the Chemical Society of Japan,* **1974**, *47*, 3049-3056. [Crossref], [Google Scholar], [Publisher]
[24] M. Arvand, Z. Lashkari, *Spectrochimica Acta Part A: Molecular and Biomolecular Spectroscopy*, 2013, 107, 280. [Crossref], [Google Scholar], [Publisher]
[25] A. Uzoukwu, K. Gloe, H. Duddeck, *Synth. React. Inorg. Met.-Org. Chem*., **1998**, *28*, 819-831. [Crossref], [Google Scholar], [Publisher]
[26] M. Asadi, S. Esmaielzadeh, K. Mohammadi, *Phosphorus, Sulfur, and Silicon*, 2010, 185, 1445–1454. [Crossref], [Google Scholar], [Publisher]
[27] A.I. Adeogun, N.W. Odozi, N.O. Obiegbedi, O.S. Bello, *African Journal of Biotechnology*, **2008**, *7*, 2736-2738. [Crossref], [Google Scholar], [Publisher]
[28] A.H. Kianfara, S. Zargarib, H.R. Khavasic, *J. Iran. Chem. Soc*., **2010**, *7*, 908-916. [Crossref], [Google Scholar], [Publisher]
[29] J. Xia, Z. Zhuo, W. Li, H.-Q. Zhang, C. Redshaw, W.H. Sun, *Inorganic Chimica Acta*., **2012**, *394*, 569-575. [Crossref], [Google Scholar], [Publisher]
[30] R. Arab Ahmadi, F. Hasanvand, G. Bruno, H. Amiri Rudbari, S. Amani, *Hindawi Publishing Corporation ISRN Inorganic Chemistry*, **2013**, *2013*, Article ID 426712. [Crossref], [Google Scholar], [Publisher]

[31] M.J. Li, T.Y. Lan, X.H. Cao, H.H. Yang, Y. Shi, C. Yi, G.N. Chen, *Dalton Transactions*, **2014**, *43*, 2789. [Crossref], [Google Scholar], [Publisher]
[32] W.S. Abdul-hassan, (Doctoral dissertation, Université Grenoble Alpes), 2018. [Crossref], [Google Scholar], [Publisher]
[33] W.S. Abdul-Hassan, E. Saint-Aman, G. Royal, C. Kahlfuss, C. Bucher, *L'Actualité Chimique*, **2018**, *430*, 79. [Crossref], [Google Scholar], [Publisher]
[34] J. Courtois, B. Wang, W. S. Abdul-hassan, L. Almasy, M. Yan, G. Royal, *Inorganic Chemistry*, **2020**, *59*, 6100. [Crossref], [Google Scholar], [Publisher]
[35] T. Sakano, F. Ito, T. Ono, O. Hirata, M. Ozawa, T. Nagamura, *Thin Solid Films*, **2010**, *519*, 1458. [Crossref], [Google Scholar], [Publisher]
[36] C. Kahlfuss, A. Milet, J. Wytko, J. Weiss, E. Saint-Aman, C. Bucher, *Organic letters*, **2015**, *17*, 4058-4061. [Crossref], [Google Scholar], [Publisher]

How to cite this article: Israa. A. Jassem, Wathiq. S. Abdul-Hassan*, Ibrahim A. Flafel, Hussein. O. Jghebil. Axial ligation for copper (II) complexes of bis (acetylacetonato) ethylenediimine and bis (3-chloroacetylacetonato) ethylenediimine. *Eurasian Chemical Communications*, 2023, 5(2), 173-203. **Link:** https://www.echemcom.com/article_159601.html